Stokes flow in a rectangular cavity by rotlet forcing

Stokes flow in a rectangular cavity by rotlet forcing

D. van der Woude, H. J. H. Clercx, and G. J. F. van Heijst
Department of Physics, Eindhoven University of Technology, 5600 MB Eindhoven, The Netherlands

V. V. Meleshko
Department of Theoretical and Applied Mechanics, Kiev National Taras Shevchenko University, 01033 Kiev, Ukraine

(Received 24 October 2006; accepted 18 April 2007; published online 14 August 2007)

The Stokes flow inside a two-dimensional rectangular cavity $|x| \leqslant a$, $|y| \leqslant b$ is analyzed for a highly viscous, incompressible fluid flow, driven by a single rotlet placed at position $(0,c)$. Specifically, a rigorous solution of the governing two-dimensional biharmonic equation for the stream function is constructed analytically by means of the superposition principle. With this solution, multicellular flow patterns can be described for narrow cavities, in which the number of flow cells is directly related to the value of the aspect ratio $A=b/a$. The solution also shows that for a certain rotlet position $(0,c_0)$, which depends on a and b, the flow has a stagnation point $(0,-c_0)$ symmetrically placed inside the rectangle. As the flow would not be affected by placing a second (inactive) rotlet in this stagnation point, this allows us to construct a blinking rotlet model for the rectangular cavity, with the inactive rotlet in the stagnation point of the flow induced by the active rotlet. For rectangular cavities, it holds that more than one of these special rotlet positions can be found for cavities that are elongated to sufficiently large aspect ratios. The blinking rotlet model is applied to illustrate several aspects of stirring in a Stokes flow in a rectangular domain. © *2007 American Institute of Physics*. [DOI: 10.1063/1.2742679]

I. INTRODUCTION

In many physical, technological, and biological systems, viscosity-dominated flows can be found. The propulsion of micro-organisms, viscous mixing processes in the chemical industry, or in the mantle of the Earth are just a few examples of creeping flow systems. Within a simplified formulation, such systems can be studied systematically using techniques from applied mathematics. In this paper, flow properties of a low Reynolds number flow confined in a closed two-dimensional rectangular domain form the central system of consideration. The situation is as follows. An incompressible, highly viscous fluid is confined in a rectangular cavity with fixed, impenetrable walls. Inside the cavity, the fluid is driven by a thin, rotating cylinder with its axis of rotation perpendicular to the fluid plane, thus resulting in a two-dimensional creeping flow. To answer the question of how the flow will be affected by the presence of the walls, and in particular by the cavity's aspect ratio, it is necessary to have access to an accurate description of the velocity field.

In the mathematical analysis of the problem, the cylinder is reduced by a limiting process to a singular stirring device: a rotlet. In this process, the rotlet's velocity field is understood as the axisymmetric steady viscous flow around a cylinder with radius R and angular velocity Ω in the limit $R \downarrow 0$ and $\Omega \to \infty$, such that $\sigma := \Omega R^2$ has a finite value.[1] The quantity σ is a measure of the fluid forcing and is denoted as the rotlet intensity or rotlet strength. The position of the rotlet is chosen arbitrarily on the long axis of the rectangular cavity. With this definition, a rotlet may be regarded as the viscous equivalent of a point vortex in inviscid fluids: both are idealized stirrers with a singular nature, producing a flow field in which the local velocity vector is tangential and is inversely proportional to the distance from the center, although the mechanism by which the fluid is brought to motion is obviously different. An interesting issue concerns the comparison of the viscous flow induced by one or more rotlets in confined circular, square, or rectangular cavities with the flow generated by one or more rotating real cylinders in such domains.

It is well known that this type of slow moving, viscosity-dominated flow is described by the two-dimensional biharmonic equation for the stream function.[2] In the particular case of a rotlet-driven Stokes flow, the biharmonic equation can be solved analytically with an exact description of the stream function as a result. With that result, accurate knowledge of the flow field is not only directly available, it is also of great use. This applies, for example, to studies of kinematic transport of tracer particles. In those cases, the flow can now be controlled and used as a given input variable, with the advantage that one can focus directly on the effects it has on the tracer transport itself. Therefore, a significant part of this paper (Sec. II) is concerned with the construction of the exact solution of this fourth-order differential equation, satisfying no-slip boundary conditions at all four impenetrable walls.

The linearity of the biharmonic equation is used to construct a solution in terms of a sum of ordinary Fourier series on the complete system of trigonometric functions in x and y coordinates. The origin of this superposition method for the rectangular domain in two dimensions can be found in the theory of elasticity and in the theory of bending plates, and has an impressive history. It started with the famous lectures of Lamé[3] and was developed among others by Mathieu,[4–6]

Koialovich,[7] Bubnov,[8,9] Lauricella,[10] Hencky,[11] and Inglis[12]—see, e.g., classical textbooks[13–15] and a review paper[16] for a detailed list of references. After that, the method was successfully applied to fluid mechanical problems, in particular to problems concerning Stokes flows in rectangular[17] and wedge cavities.[18] In Ref. 17, the flow was driven by tangentially moving top and bottom walls and it was demonstrated that the superposition principle is extremely useful in deriving an analytical expression of the velocity field for this kind of cavity flow, fulfilling the imposed boundary conditions identically. The principles of this construction technique are adopted and applied successfully in the analysis of the Stokes flow produced by a single rotlet. Although the bounding walls in the present problem are essentially not moving, the formulation of the problem can be transformed into one that involves an auxiliary stream function that has to satisfy nonzero tangential and normal wall velocities imposed at all four walls, instead of two as in Ref. 17. In comparison with the study of Meleshko,[17] the complexity of the problems has increased. In adjusting the auxiliary solution to the boundary condition, a system of two coupled infinite series, containing known and unknown Fourier coefficients in a complicated manner, has to be solved. Here the system is evaluated numerically by using the method of successive approximation, which is rapidly convergent. An alternative algorithm could be the method of reduction as described in Refs. 19 and 20.

In Secs. III and IV, the practical value of solving the biharmonic equation is illustrated by employing the result in a qualitative study on multicellular flow structures (Sec. III) and on chaotic advection of tracer particles in a time-dependent viscous flow (Sec. IV). In the first application, the steady-state flow patterns inside a rectangular cavity are examined. By plotting the stream function for several values of the aspect ratio of the cavity, a multicellular flow structure becomes visible for narrow cavity geometries. The existence of similar structures was already reported by Hellou and Coutanceau[21] and Jana, Metcalfe, and Ottino.[22] Hellou and Coutanceau[21] describe a configuration that is similar to the rotlet configuration in that the agitation of the fluid is executed by an internal forcing mechanism. There, a rotating circular cylinder is set in the center of the cavity and is responsible for an array of single-core cells which number is determined by the aspect ratio $A=b/a\geqslant 1$, with $2a$ the width and $2b$ the length of the cavity. By increasing the value of A gradually, it was shown numerically and experimentally how these cells develop and how they are formed in a merging process of two main corner cells.

A different pattern is found when a second rotlet is added to the problem. Forcing the fluid with two spatially separated rotlets gives rise to a flow that differs from the single rotlet case by the existence of a double-core central cell, of which the structure depends on the direction of rotation of the individual rotlets. Related to that is the computational and experimental study of Jana *et al.*[22] on mixing in Stokes flows, in which a viscous cavity flow is described that is completely determined by an externally assigned tangential moving top and bottom wall. For two active rotlets, besides the presence of a double-core central cell, it was demonstrated that a multicellular structure can be found when the cavity is elongated to sufficiently large aspect ratios.

Section IV deals with chaotic advection in time-dependent viscous flows. By adding a second, individually adjustable rotlet to the problem, a blinking rotlet model can be constructed. This means that both rotlets are switched "on" and "off" periodically, but such that only one rotlet is active at a time. Since the pioneering work of Aref[23] more than two decades ago, it has been widely recognized that complex particle trajectories not only occur in high-Reynolds number turbulent flows, but also in laminar flows and even in viscosity-dominated (Stokes) flows. From dynamical systems theory, it is well known that a system is nonintegrable if the system has more than one degree of freedom. In a two-dimensional system, the governing equations for particle trajectories in an incompressible flow form a dynamical system in Hamiltonian form, where the stream function plays the role of the Hamiltonian. As opposed to steady flows, which have only one degree of freedom and are intrinsically nonchaotic, a time-dependent flow has the necessary extra degree of freedom by which it can produce complex particle trajectories. In chaotically behaving flows, a patch of passive fluid is deformed considerably by successive stretching and folding during the evolution of the flow. This chaotic nature may be characterized by an exponential growth in time of the contact length of the patch with its surroundings. This means that even in a two-dimensional laminar environment, chaotic transport is possible and time dependency is an essential ingredient in "good stirring."

An alternative method to create chaotic creeping flows was employed by Otto, Yannacopoulos, and Blake.[24] Instead of alternating active rotlets, they considered forcing by a blinking Stokeslet for the mixing and transport processes in Stokes flow. Their study was motivated by the feeding currents induced by cilia or flagella in sessile micro-organisms, indicating the importance of studying the distributive properties of low-Reynolds number flows. In spite of this particular motivation, their paper has a generic character.

A family of two-roll-mill flows in a circular domain was investigated both numerically and experimentally by Price, Mullin, and Kobine.[25] They used two real rotating cylinders inside a stationary outer cylinder. In this study, the ratio of the angular velocities of the inner cylinders was varied, and a complete sequence of complex transitions between the extreme cases of counter- and corotation was uncovered. The change in flow topology is extensively discussed, and they have identified all the critical topological transitions occurring in the flow during the change from fully counter-rotating cylinders to fully corotating cylinders. This combined numerical and experimental investigation is restricted to the circular domain and no results in the same spirit have been reported for rectangular cavities, although Moreau and Bourot[26] have considered the case of two-dimensional Stokes flow driven by two cylinders in an unbounded rectilinear channel. In their numerical study, the cylinders were situated on a line perpendicular to the channel boundaries. A similar numerical study of Stokes flows and associated mixing properties induced by rotating cylinders in square and rectangular cavities might provide an interesting connection

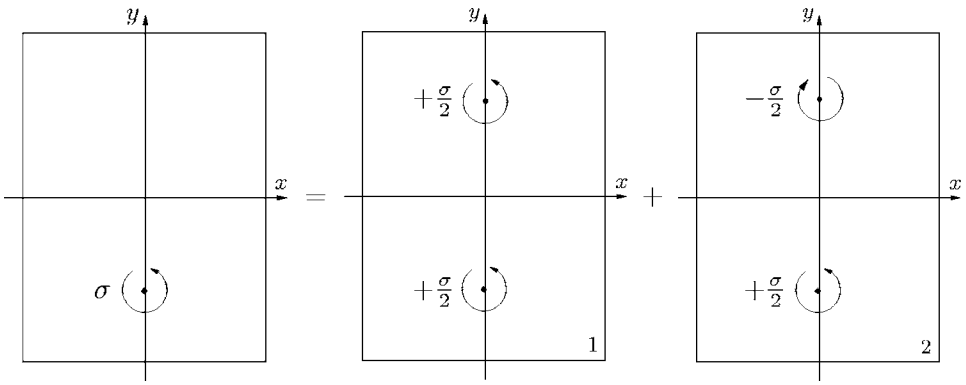

FIG. 1. The flow field associated with the single rotlet is decomposed into two flow fields associated with two corotating and counter-rotating rotlets, respectively, described by the elemental stream functions Ψ_1 and Ψ_2.

with the work by Hellou and Coutanceau[21] and the present study.

The blinking rotlet model was introduced by Meleshko and Aref[1] as an alternative for the classical blinking vortex model when discussing chaotic advection in Stokes flow. In their study, the flow region is restricted by the boundary of a circle, and, although there are some similarities with the present work, the difference in geometry reveals a different stirring pattern, making it worthwhile to study the problem of a Stokes flow in a rectangular cavity. The possibility of changing the aspect ratio of the domain dimensions appears to be of great influence of the internal flow field and stirring properties. The presence of an internal stagnation point, located symmetrically with respect to the rotlet position, was pointed out in Ref. 1 and allows a blinking rotlet model in which the rotlet that is "off" does not disturb the flow generated by the rotlet that is "on." This important feature also holds for rotlet flows in slender cavities. But more importantly, it turns out that for certain aspect ratios, several of these special rotlet positions can be found. How different rotlet positions will influence the stirring quality of the model is studied numerically by observing the deformation in time of the boundary of a passive blob. For that purpose, the advection of a number of boundary nodes is calculated by integrating the Lagrangian equations of motion with a Runge-Kutta method with variable time step and order (see Hairer, Nørsett, and Wanner[27]). The integration scheme is area-preserving. Finally, Sec. V summarizes the most important findings and results.

II. STOKES FLOW BY A SINGLE ROTLET

Consider a two-dimensional Stokes flow of an incompressible fluid in a rectangular cavity $|x|<a$, $|y|<b$ with rigid, fixed walls. The fluid is driven by a single rotlet with strength σ, which is placed on the y axis at $(0,-c)$.

In terms of the stream function $\Psi(x,y)$, the components of the velocity field are given by

$$u = \frac{\partial \Psi}{\partial y}, \quad v = -\frac{\partial \Psi}{\partial x}. \tag{1}$$

In the absence of the inertia terms, the steady-state equation of motion reduces to the two-dimensional biharmonic equation for Ψ,

$$\frac{\partial^4 \Psi}{\partial x^4} + 2\frac{\partial^4 \Psi}{\partial x^2 \partial y^2} + \frac{\partial^4 \Psi}{\partial y^4} = 0, \tag{2}$$

which must be satisfied in the whole domain except for the rotlet's point $(0,-c)$. At the boundaries, the condition of zero velocity leads to homogeneous conditions for Ψ,

$$\Psi = 0, \quad \frac{\partial \Psi}{\partial x} = 0, \quad x = \pm a, \quad |y| \leqslant b, \tag{3a}$$

$$\Psi = 0, \quad \frac{\partial \Psi}{\partial y} = 0, \quad |x| \leqslant a, \quad y = \pm b. \tag{3b}$$

Instead of solving the biharmonic equation for the overall stream function Ψ directly, the linearity of the equation is used in order to split Ψ into two so-called elemental stream functions Ψ_1 and Ψ_2, such that

$$\Psi(x,y) = \Psi_1(x,y) + \Psi_2(x,y). \tag{4}$$

Each of the elemental stream functions satisfies the homogeneous biharmonic equation (2). From a physical point of view, the stream function Ψ_1 represents a steady viscous flow generated by two simultaneously active corotating rotlets of intensity $\sigma/2$ located at the points $(0,-c)$ and $(0,c)$. Therefore, Ψ_1 is an even function in both the x and y coordinates. When, on the other hand, the fluid is stirred by two simultaneously active counter-rotating rotlets of intensity $\pm\sigma/2$ located at the points $(0,-c)$ and $(0,c)$, respectively, the stream function, now denoted by Ψ_2, is an even function in x and an odd function in the y coordinate. In Fig. 1, the decomposition of Ψ in terms of the elemental functions Ψ_1 and Ψ_2 is shown graphically. The mathematical reason for making this decomposition lies in the fact that certain symmetry properties in the subproblems 1 and 2 arise in which the parity of the elemental stream functions can easily be employed in constructing the solution of the full problem.

A. Problem 1

In problem 1, the creeping flow is created by two corotating rotlets, each of intensity $\sigma/2$ and symmetrically placed on the y axis at points $(0,c)$ and $(0,-c)$. By using the definition of a single rotlet, the rotlet stream function $\psi_1^{(\sigma)}$ for this problem is readily found; it has two logarithmic singularities and is given by

$$\psi_1^{(\sigma)}(x,y) = \frac{\sigma}{4}\ln[x^2+(y+c)^2] + \frac{\sigma}{4}\ln[x^2+(y-c)^2]. \quad (5)$$

Obviously, the solution (5) does not satisfy the condition of zero velocity at the walls. Therefore, a second stream function ψ_1 is introduced, which can be determined analytically by using the linearity of the problem, in writing Ψ_1 as the sum of the preceding contributions

$$\Psi_1(x,y) = \psi_1(x,y) + \psi_1^{(\sigma)}(x,y). \quad (6)$$

With the particular form of $\psi_1^{(\sigma)}$, expressing the irrotational nature of the direct rotlet flow, it follows that $\nabla^2\psi_1^{(\sigma)}=0$ in the entire domain, except at the singularities. Since Ψ_1 is a solution of the two-dimensional biharmonic equation, the unknown function ψ_1 is that as well. By shifting the focus from the overall stream function Ψ_1 to the auxiliary function ψ_1, the zero-velocity boundary condition imposed on Ψ_1 is translated into inhomogeneous conditions for ψ_1,

$$\frac{\partial\psi_1}{\partial x} = \mp V_1(y), \quad \psi_1 = -g_1(y), \quad x = \pm a, \quad |y| \leqslant b,$$
$$\frac{\partial\psi_1}{\partial y} = \mp U_1(x), \quad \psi_1 = -f_1(x), \quad y = \pm b, \quad |x| \leqslant a. \quad (7)$$

It is seen that the homogeneous conditions of (3) are transferred into a mixed set of inhomogeneous boundary conditions of the Neumann and Dirichlet type. Here, the assigned functions at the walls follow from the rotlet stream function $\psi_1^{(\sigma)}$ evaluated at the boundaries,

$$V_1(y) = \frac{\sigma}{2}\left[\frac{a}{a^2+(y+c)^2} + \frac{a}{a^2+(y-c)^2}\right], \quad (8a)$$

$$f_1(x) = \frac{\sigma}{4}\ln[x^2+(b+c)^2] + \frac{\sigma}{4}\ln[x^2+(b-c)^2], \quad (8b)$$

$$g_1(y) = \frac{\sigma}{4}\ln[a^2+(y+c)^2] + \frac{\sigma}{4}\ln[a^2+(y-c)^2], \quad (8c)$$

$$U_1(x) = \frac{\sigma}{2}\left[\frac{(b+c)}{x^2+(b+c)^2} + \frac{(b-c)}{x^2+(b-c)^2}\right]. \quad (8d)$$

These even functions are infinitely differentiable and can be presented in the form of the Fourier series,

$$V_1(y) = \sum_{l=1}^{\infty}(-1)^l V_l^{(1)}\cos(\beta_l y),$$
$$V_l^{(1)} = \frac{(-1)^l}{b}\int_{-b}^{b} V_1(y)\cos(\beta_l y)dy, \quad (9a)$$

$$f_1(x) = \sum_{m=1}^{\infty}(-1)^m f_m^{(1)}\cos(\alpha_m x),$$
$$f_m^{(1)} = \frac{(-1)^m}{a}\int_{-a}^{a} f_1(x)\cos(\alpha_m x)dx, \quad (9b)$$

$$g_1(y) = \sum_{l=1}^{\infty}(-1)^l g_l^{(1)}\cos(\beta_l y),$$
$$g_l^{(1)} = \frac{(-1)^l}{b}\int_{-b}^{b} g_1(y)\cos(\beta_l y)dy, \quad (9c)$$

$$U_1(x) = \sum_{m=1}^{\infty}(-1)^m U_m^{(1)}\cos(\alpha_m x),$$
$$U_m^{(1)} = \frac{(-1)^m}{a}\int_{-a}^{a} U_1(x)\cos(\alpha_m x)dx. \quad (9d)$$

The constants α_m and β_l are defined as

$$\alpha_m = \frac{(2m-1)\pi}{2a} \quad \text{and} \quad \beta_l = \frac{(2l-1)\pi}{2b}. \quad (10)$$

The leading terms of the Fourier coefficients are

$$V_l^{(1)} = -\frac{2V_1(b)}{b\beta_l} + \frac{2V_1''(b)}{b\beta_l^3} + \frac{(-1)^l}{b\beta_l^4}\int_{-b}^{b} V_1^{(\mathrm{IV})}(y)\cos(\beta_l y)dy, \quad (11a)$$

$$f_m^{(1)} = -\frac{2f_1(a)}{a\alpha_m} + \frac{2f_1''(a)}{a\alpha_m^3} - \frac{2f_1^{(\mathrm{IV})}(a)}{a\alpha_m^5} - \frac{(-1)^m}{a\alpha_m^5}\int_{-a}^{a} f_1^{(\mathrm{V})}(x)\times\sin(\alpha_m x)dx, \quad (11b)$$

$$g_l^{(1)} = -\frac{2g_1(b)}{b\beta_l} + \frac{2g_1''(b)}{b\beta_l^3} - \frac{2g_1^{(\mathrm{IV})}(b)}{b\beta_l^5} - \frac{(-1)^l}{b\beta_l^5}\int_{-b}^{b} g_1^{(\mathrm{V})}(y)\times\sin(\beta_l y)dy, \quad (11c)$$

$$U_m^{(1)} = -\frac{2U_1(a)}{a\alpha_m} + \frac{2U_1''(a)}{a\alpha_m^3} + \frac{(-1)^m}{a\alpha_m^4}\int_{-a}^{a} U_1^{(\mathrm{IV})}(x)\times\cos(\alpha_m x)dx. \quad (11d)$$

The unknown function ψ_1 is found by means of the method of superposition[17] by writing ψ_1 as a sum of four ordinary Fourier series,

$$\psi_1(x,y) = b\sum_{m=1}^{\infty}\frac{(-1)^m}{\alpha_m}X_m^{(1)}P_m^{(1)}(y)\cos(\alpha_m x) - a\sum_{l=1}^{\infty}\frac{(-1)^l}{\beta_l}Y_l^{(1)}Q_l^{(1)}(x)\cos(\beta_l y) - \sum_{m=1}^{\infty}(-1)^m f_m^{(1)}\frac{\cosh(\alpha_m y)}{\cosh(\alpha_m b)}\cos(\alpha_m x) - \sum_{l=1}^{\infty}(-1)^l g_l^{(1)}\frac{\cosh(\beta_l x)}{\cosh(\beta_l a)}\cos(\beta_l y). \quad (12)$$

Here the even functions $P_m^{(1)}(y)$ and $Q_l^{(1)}(x)$ are given by

$$P_m^{(1)}(y) = b\tanh(\alpha_m b)\frac{\cosh(\alpha_m y)}{\cosh(\alpha_m b)} - y\frac{\sinh(\alpha_m y)}{\cosh(\alpha_m b)},$$

$$Q_l^{(1)}(x) = a\tanh(\beta_l a)\frac{\cosh(\beta_l x)}{\cosh(\beta_l a)} - x\frac{\sinh(\beta_l x)}{\cosh(\beta_l a)}. \tag{13}$$

Each term of the series satisfies the biharmonic equation and the whole representation has enough functional arbitrariness in terms of the Fourier coefficients $X_m^{(1)}$ and $Y_l^{(1)}$ to fulfil all boundary conditions formulated in (7). In order to determine $X_m^{(1)}$ and $Y_l^{(1)}$ in accordance with the boundary condition for the normal derivatives, the following expansions (see Hansen[28] and Oberhettinger[29]) are applied to rewrite expression (12):

$$\frac{\cosh(\nu z)}{\cosh(\nu L)} = -\frac{2}{L}\sum_{p=1}^{\infty}(-1)^p\frac{\lambda_p}{\nu^2+\lambda_p^2}\cos(\lambda_p z), \quad -L<z<L, \tag{14}$$

$$L\tanh(\nu L)\frac{\cosh(\nu z)}{\cosh(\nu L)} - z\frac{\sinh(\nu z)}{\cosh(\nu L)} = -\frac{4\nu}{L}\sum_{p=1}^{\infty}(-1)^p\frac{\lambda_p\cos(\lambda_p z)}{(\nu^2+\lambda_p^2)^2}, \quad -L\leqslant z\leqslant L. \tag{15}$$

Here ν is an arbitrary constant; μ_p and λ_p are given by

$$\mu_p = \frac{p\pi}{L}, \quad \lambda_p = \frac{(2p-1)}{2L}\pi, \quad p = 1,2,3,\ldots.$$

The result can be rearranged leading to an infinite system of linear algebraic equations for the unknown coefficients $X_m^{(1)}$ and $Y_l^{(1)}$,

$$X_m^{(1)} b\Delta_1(\alpha_m b) - \sum_{l=1}^{\infty} Y_l^{(1)}\frac{4\alpha_m^2\beta_l}{(\alpha_m^2+\beta_l^2)^2} = H_m^{(1)}, \quad m = 1,2,\ldots, \tag{16a}$$

$$Y_l^{(1)} a\Delta_1(\beta_l a) - \sum_{m=1}^{\infty} X_m^{(1)}\frac{4\beta_l^2\alpha_m}{(\beta_l^2+\alpha_m^2)^2} = I_l^{(1)}, \quad l = 1,2,\ldots. \tag{16b}$$

In this expression, the shorthand notation $\Delta_1(\xi)$ is introduced,

$$\Delta_1(\xi) = \tanh(\xi) + \frac{\xi}{\cosh^2(\xi)}. \tag{17}$$

The free terms $H_m^{(1)}$ and $I_l^{(1)}$ collect all the known coefficients and are given by

$$H_m^{(1)} = \alpha_m^2\left(\frac{2}{a}\sum_{l=1}^{\infty} g_l^{(1)}\frac{\beta_l}{\alpha_m^2+\beta_l^2} - f_m^{(1)}\tanh(\alpha_m b) + \frac{U_m^{(1)}}{\alpha_m}\right), \tag{18}$$

$$I_l^{(1)} = -\beta_l^2\left(\frac{2}{b}\sum_{m=1}^{\infty} f_m^{(1)}\frac{\alpha_m}{\beta_l^2+\alpha_m^2} - g_l^{(1)}\tanh(\beta_l a) + \frac{V_l^{(1)}}{\beta_l}\right). \tag{19}$$

By combining the expressions for the Fourier coefficients (9c) and (9b) and the Fourier expansion (14), one can write

$$2\sum_{l=1}^{\infty} g_l^{(1)}\frac{\beta_l}{\alpha_m^2+\beta_l^2} = \int_{-b}^{b} g_1(y)\left[\frac{2}{b}\sum_{l=1}^{\infty}(-1)^l\frac{\beta_l}{\alpha_m^2+\beta_l^2}\cos(\beta_l y)\right]dy = -\int_{-b}^{b} g_1(y)\frac{\cosh(\alpha_m y)}{\cosh(\alpha_m b)}dy,$$

$$2\sum_{m=1}^{\infty} f_m^{(1)}\frac{\alpha_m}{\beta_l^2+\alpha_m^2} = \int_{-a}^{a} f_1(x)\left[\frac{2}{a}\sum_{m=1}^{\infty}(-1)^m\frac{\alpha_m}{\beta_l^2+\alpha_m^2}\cos(\alpha_m x)\right]dx = -\int_{-a}^{a} f_1(x)\frac{\cosh(\beta_l x)}{\cosh(\beta_l a)}dx.$$

Next, integrating these expressions by parts and using the representations (11), the result for $H_m^{(1)}$ reads after some algebra

$$\begin{aligned} H_m^{(1)} = {} & \frac{2}{a}\alpha_m[f_1(a)-g_1(b)]\tanh(\alpha_m b) + \frac{2}{a}[g_1'(b)-U_1(a)] \\ & - \frac{2}{a\alpha_m}[f_1''(a)+g_1''(b)]\tanh(\alpha_m b) + \frac{2}{a\alpha_m^2}[g_1'''(b)+U_1''(a)] \\ & + \frac{2}{a\alpha_m^3}[f_1^{(\mathrm{IV})}(a)-g_1^{(\mathrm{IV})}(b)]\tanh(\alpha_m b) \\ & + \frac{(-1)^m}{a\alpha_m^3}\int_{-a}^{a}[U_1^{(\mathrm{IV})}(x)\cos(\alpha_m x) + f_1^{(\mathrm{V})}(x) \\ & \times\tanh(\alpha_m b)\sin(\alpha_m x)]dx + \frac{1}{a\alpha_m^3}\int_{-b}^{b} g_1^{(\mathrm{V})}(y) \\ & \times\frac{\sinh(\alpha_m y)}{\cosh(\alpha_m b)}dy. \end{aligned} \tag{20}$$

Because all terms within square brackets vanish according to the definitions (8), we finally find that

$$\begin{aligned} H_m^{(1)} = {} & \frac{(-1)^m}{a\alpha_m^3}\int_{-a}^{a}[U_1^{(\mathrm{IV})}(x)\cos(\alpha_m x) + f_1^{(\mathrm{V})}(x) \\ & \times\tanh(\alpha_m b)\sin(\alpha_m x)]dx + \frac{1}{a\alpha_m^3}\int_{-b}^{b} g_1^{(\mathrm{V})}(y) \\ & \times\frac{\sinh(\alpha_m y)}{\cosh(\alpha_m b)}dy = \mathcal{O}(m^{-4}), \quad m\to\infty. \end{aligned} \tag{21}$$

On similar grounds, $I_l^{(1)}$ may be written as

$$I_l^{(1)} = -\frac{(-1)^l}{b\beta_l^3}\int_{-a}^{a}[V_1^{(\mathrm{IV})}(y)\cos(\beta_l y) + g_1^{(\mathrm{V})}(y) \times \tanh(\beta_l a)\sin(\beta_l y)]dy - \frac{1}{b\beta_l^3}\int_{-a}^{a} f_1^{(\mathrm{V})}(x) \times \frac{\sinh(\beta_l x)}{\cosh(\beta_l a)}dx = \mathcal{O}(l^{-4}), \quad l\to\infty. \tag{22}$$

It was shown in Ref. 20 that the coupled infinite system (16) is fully regular, that is, the sums of the outdiagonal elements in each line of (16a) and (16b) are less than the diagonal element by a finite positive value that is independent of the numbers m and l. According to the general theory,[19] these infinite system can be solved by employing the method of successive approximation. We state that the coefficients $X_m^{(1)}$ and $Y_n^{(1)}$ can be written as a sum,

$$X_m^{(1)} = X_{m0}^{(1)} + X_{m1}^{(1)} + X_{m2}^{(1)} + \cdots, \quad m = 1,2,3,\ldots,$$

$$Y_l^{(1)} = Y_{l0}^{(1)} + Y_{l1}^{(1)} + Y_{l2}^{(1)} + \cdots, \quad l = 1,2,3,\ldots.$$

Here, the zeroth-order contributions $X_{m0}^{(1)}$ and $Y_{l0}^{(1)}$ are connected to the free terms via

$$X_{m0}^{(1)} = \frac{H_m^{(1)}}{b\Delta_1(\alpha_m b)}, \quad Y_{l0}^{(1)} = \frac{I_l^{(1)}}{a\Delta_1(\beta_l a)}.$$

Then, the higher-order contributions follow from a simple summation routine,

$$X_{ms}^{(1)} b\Delta_1(\alpha_m b) = \sum_{l=1}^{\infty} Y_{l(s-1)}^{(1)} \frac{4\alpha_m^2\beta_l}{(\alpha_m^2+\beta_l^2)^2}, \quad m,s = 1,2,3,\ldots,$$

$$Y_{ls}^{(1)} a\Delta_1(\beta_l a) = \sum_{m=1}^{\infty} X_{m(s-1)}^{(1)} \frac{4\beta_l^2\alpha_m}{(\beta_l^2+\alpha_m^2)^2}, \quad l,s = 1,2,3,\ldots.$$

More important is the asymptotic behavior of the coefficients with large numbers of indices, which was established in Ref. 20 by using the asymptotic behavior of the free terms expressed in (21) and (22),

$$X_m^{(1)} = \frac{E_1}{\alpha_m} + \mathrm{Re}\left(\frac{E_1^{(\gamma)}}{\alpha_m^{\gamma}}\right), \quad m\to\infty,$$

$$Y_l^{(1)} = \frac{E_1}{\beta_l} - \mathrm{Re}\left(\frac{E_1^{(\gamma)}}{\beta_l^{\gamma}}\right), \quad l\to\infty, \tag{23}$$

where $E_1^{(\gamma)}$ is a complex-valued constant, and $\gamma = 2.739593 + i1.119025$ is the root of the transcendental equation

$$\sin\frac{\pi\gamma}{2} + \gamma = 0, \tag{24}$$

with the lowest real part (the root is not exact, and the accuracy is indicated by the number of digits). Obviously, more roots of (24) are possible. The reason for this particular choice is related to the asymptotic behavior of the coefficients $X_m^{(1)}$ and $Y_l^{(1)}$, as explained in detail by Meleshko and Gomilko.[20] The real-valued constant E_1 is determined by

$$\frac{\pi}{2ab}E_1 = \sum_{m=1}^{\infty} H_m^{(1)} + \sum_{l=1}^{\infty} I_l^{(1)}. \tag{25}$$

When we use the relations

$$\frac{1}{L}\sum_{p=1}^{\infty}\frac{(-1)^p}{\lambda_p^3}\cos(\lambda_p z) = \frac{1}{4}[z^2 - L^2], \quad -L\le z\le L,$$

$$\frac{1}{L}\sum_{p=1}^{\infty}\frac{(-1)^p}{\lambda_p}\cos(\lambda_p z) = -\frac{1}{2}, \quad -L < z < L, \tag{26}$$

$$\sum_{m=1}^{\infty}\frac{1}{a\alpha_m^2}\frac{\cosh(\alpha_m y)}{\cosh(\alpha_m b)} - \sum_{l=1}^{\infty}\frac{(-1)^l}{b\beta_l^2}\tanh(\beta_l a)\cos(\beta_l y) = \frac{a}{2}, \tag{27}$$

and

$$\sum_{l=1}^{\infty}\frac{1}{b\beta_l^2}\frac{\cosh(\beta_l x)}{\cosh(\beta_l a)} - \sum_{m=1}^{\infty}\frac{(-1)^m}{a\alpha_m^2}\tanh(\alpha_m b)\cos(\alpha_m x) = \frac{b}{2}, \tag{28}$$

then, after some tedious algebra, we obtain that the sum on the right-hand side of (25) is identically equal to zero, and, consequently, $E_1 = 0$.

In order to improve the convergence of the stream function, new coefficients, related to $f_m^{(1)}$ and $g_l^{(1)}$, are introduced,

$$\bar{f}_m^{(1)} = f_m^{(1)} + \frac{2f_1(a)}{a\alpha_m} - \frac{2f_1''(a)}{a\alpha_m^3} = -\frac{2f_1^{(\mathrm{IV})}(a)}{a\alpha_m^5} - \frac{(-1)^m}{a\alpha_m^5}\int_{-a}^{a} f_1^{(\mathrm{V})}(x) \times \sin(\alpha_m x)dx = \mathcal{O}(m^{-4}), \quad m\to\infty, \tag{29}$$

$$\bar{g}_l^{(1)} = g_l^{(1)} + \frac{2g_1(b)}{b\beta_l} - \frac{2g_1''(b)}{b\beta_l^3} = -\frac{2g_1^{(\mathrm{IV})}(b)}{b\beta_l^5} - \frac{(-1)^l}{b\beta_l^5}\int_{-b}^{b} g_1^{(\mathrm{V})}(y) \times \sin(\beta_l y)dy = \mathcal{O}(l^{-4}), \quad l\to\infty. \tag{30}$$

Hence, the final representation for the stream function Ψ_1 reads

$$\Psi_1(x,y) = b\sum_{m=1}^{\infty}\frac{(-1)^m}{\alpha_m}X_m^{(1)}P_m^{(1)}(y)\cos(\alpha_m x) - a\sum_{l=1}^{\infty}\frac{(-1)^l}{\beta_l}Y_l^{(1)}Q_l^{(1)}(x)\cos(\beta_l y) - \sum_{m=1}^{\infty}(-1)^m\bar{f}_m^{(1)}\frac{\cosh(\alpha_m y)}{\cosh(\alpha_m b)}\cos(\alpha_m x) - \sum_{l=1}^{\infty}(-1)^l\bar{g}_l^{(1)}\frac{\cosh(\beta_l x)}{\cosh(\beta_l a)}\cos(\beta_l y) - C_1 + D_1\left(\frac{a^2-x^2}{2} - \frac{b^2-y^2}{2}\right) + \frac{\sigma}{4}\ln[x^2+(y+c)^2] + \frac{\sigma}{4}\ln[x^2+(y-c)^2], \tag{31}$$

TABLE I. Numerical values of the first eight free terms and expansion coefficients of problem 1 for the case in which $a=1$, $b=4$,and $c=2.256772$. Any value of c could be used for this purpose, provided $|c|<4$. However, the particular choice of c here is related with a few applications; see Sec. IV.

m,l	$H_m^{(1)}$	$I_l^{(1)}$	$-\alpha_m\bar{f}_m^{(1)}$	$-\beta_l\bar{g}_l^{(1)}$	$X_m^{(1)}$	$Y_l^{(1)}$
1	-0.3194630	0.1808995	-0.1231876	-0.2090062	2.5691×10^{-3}	0.2546654
2	4.0064748×10^{-3}	0.4608897	-5.7542767×10^{-3}	-0.18854587	2.8988×10^{-3}	0.3855975
3	-2.7937793×10^{-5}	-0.1178307	-2.3569776×10^{-3}	4.0640223×10^{-2}	-5.027×10^{-4}	-0.1044729
4	1.6364437×10^{-7}	-0.2743452	-1.2163433×10^{-3}	5.5281448×10^{-2}	-3.497×10^{-4}	-0.2630945
5	-8.8029144×10^{-10}	-1.9715015×10^{-2}	-7.3912857×10^{-4}	5.9057676×10^{-3}	-2.071×10^{-4}	-1.81120×10^{-2}
6	4.5015035×10^{-12}	8.55777365×10^{-2}	-4.9585787×10^{-4}	-7.8371548×10^{-3}	-1.259×10^{-4}	8.65503×10^{-2}
7	-2.2258155×10^{-14}	2.4397861×10^{-2}	-3.5545151×10^{-4}	-9.1852834×10^{-4}	-7.98×10^{-5}	2.54270×10^{-2}
8	1.0745155×10^{-16}	-1.9117824×10^{-2}	-2.6718261×10^{-4}	2.7216230×10^{-3}	-5.25×10^{-5}	-1.82171×10^{-2}

with

$$C_1 = f_1(a) = g_1(b) = \frac{\sigma}{4}\ln[a^2+(b+c)^2] + \frac{\sigma}{4}\ln[a^2+(b-c)^2]$$

and

$$D_1 = f_1''(a) = -g_1''(b) = -\frac{\sigma}{2}\left[\frac{a^2-(b+c)^2}{[a^2+(b+c)^2]^2} + \frac{a^2-(b-c)^2}{[a^2+(b-c)^2]^2}\right].$$

To obtain expression (31), we used the relations

$$\frac{2}{a}\sum_{m=1}^{\infty}\frac{(-1)^m}{\alpha_m}\frac{\cosh(\alpha_m y)}{\cosh(\alpha_m b)}\cos(\alpha_m x) + \frac{2}{b}\sum_{l=1}^{\infty}\frac{(-1)^l}{\beta_l}\frac{\cosh(\beta_l x)}{\cosh(\beta_l a)}\cos(\beta_l y) = -1 \tag{32}$$

and

$$\frac{2}{a}\sum_{m=1}^{\infty}\frac{(-1)^m}{\alpha_m^3}\frac{\cosh(\alpha_m y)}{\cosh(\alpha_m b)}\cos(\alpha_m x) - \frac{2}{b}\sum_{l=1}^{\infty}\frac{(-1)^l}{\beta_l^3}\frac{\cosh(\beta_l x)}{\cosh(\beta_l a)}\cos(\beta_l y) = \frac{b^2-y^2}{2} - \frac{a^2-x^2}{2}. \tag{33}$$

Due to the asymptotic behavior of the coefficients $X_m^{(1)}$, $Y_l^{(1)}$, given by (23) with $E_1=0$, and $\bar{f}_m^{(1)}$, $\bar{g}_l^{(1)}$, which are expressed in (29) and (30), respectively, the Fourier series in (31) converge extremely rapid in all points of the rectangle, including its boundary with corner points.

In order to give an idea of some typical values of the relevant coefficients, as well as their accuracy, Table I lists an overview of the first eight numerical values of the expansion coefficients $X_m^{(1)}$, $Y_l^{(1)}$, $\bar{f}_m^{(1)}$, and $\bar{g}_m^{(1)}$ and the free terms $H_m^{(1)}$ and $I_l^{(1)}$ in the particular case of a rectangular cavity with $a=1$, $b=4$, and rotlet position $(0,-c)=(0,-2.256772)$. For this particular choice, a rotlet located in $(0,-c)$ coincides with the stagnation point of the flow induced by a rotlet located in $(0,c)$. Thus the second, symmetrically placed rotlet does not disturb the position of the first rotlet, and vice versa. There might be more of these special positions, depending on the aspect ratio of the container (see Sec. IV for further discussion). The coefficients $-\alpha_m\bar{f}_m^{(1)}$, $-\beta_l\bar{g}_l^{(1)}$, $H_m^{(1)}$, and $I_l^{(1)}$ were calculated by evaluating the integrals expressed in (29), (30), (21), and (22) numerically with a relative error of 10^{-7}. The expansion coefficients $X_m^{(1)}$ and $Y_l^{(1)}$ are determined with an absolute error of 10^{-7} by solving the coupled infinite series (16) by means of the method of successive approximation. By varying those parameters that control the accuracy of the calculations over a wide range, the accuracy displayed in Table I was obtained.

Another important issue related with representation (31) for $\Psi_1(x,y)$ is the local behavior of the stream function near a quiet corner, say, near $x=a$, $y=b$. Since the work of Moffatt,[30] it is known that, despite the exact nature of the driving force, a creeping flow near the apex of a wedge shows a sequence of corner cells, decreasing in size and intensity when the corner is approached. Here, the solution of the local stream function, expressed in plane polar coordinates (ρ,θ), was of the form $\Psi(\rho,\theta)=\rho^\gamma f_\gamma(\theta)$. Dean and Montagnon[31] already proved that for wedge angles smaller than a certain critical angle of approximately 146°, the exponent γ is necessarily complex-valued; and it was Moffatt's merit to interpret this as the occurrence of a sequence of corner eddies. In fact, it can be shown, following Meleshko, Gomilko, and Gourjii,[32] that when the stream function is expanded in the local polar coordinates with $x=a-\rho\cos\theta$ and $y=b-\rho\sin\theta$, $\Psi_1(\rho,\theta)$ can be written in the above form and that it has indeed a complex-valued exponent. Important to notice is that the amplitude of these Moffatt eddies is explicitly related to the value of $E_\gamma^{(1)}$.

B. Problem 2

The situation in problem 2 also consists of two rotlets, still positioned at points $(0,-c)$ and $(0,c)$, but now rotating in opposite directions. Although the signs of the rotlet strengths are different, their absolute value is $\sigma/2$. The rotlet stream function $\psi_2^{(\sigma)}$, therefore, reads

$$\psi_2^{(\sigma)}(x,y) = \frac{\sigma}{4}\ln[x^2+(y+c)^2] - \frac{\sigma}{4}\ln[x^2+(y-c)^2]. \quad (34)$$

As in the previous subsection, the second elemental stream function Ψ_2 is written as a linear combination of the rotlet stream function and a function ψ_2 due to the presence of the boundaries

$$\Psi_2(x,y) = \psi_2(x,y) + \psi_2^{(\sigma)}(x,y). \quad (35)$$

Because the second elemental stream function Ψ_2 is a solution of the linear biharmonic equation, ψ_2 is forced to be a solution of the biharmonic equation as well, although with adjusted boundary conditions. The requirement of zero velocities perpendicular and tangentially to the cavity walls implies the following boundary conditions:

$$\frac{\partial\psi_2}{\partial x} = \mp V_2(y), \quad \psi_2 = -g_2(y), \quad x = \pm a, \quad |y| \leqslant b,$$
$$\frac{\partial\psi_2}{\partial y} = -U_2(y), \quad \psi_1 = \mp f_2(x), \quad y = \pm b, \quad |x| \leqslant a. \quad (36)$$

The functions V_2 and g_2 are odd functions in their argument, whereas U_2 and f_2 are even functions. They follow directly from the rotlet solution (34),

$$V_2(y) = \frac{\sigma}{2}\left[\frac{a}{a^2+(y+c)^2} - \frac{a}{a^2+(y-c)^2}\right], \quad (37a)$$

$$f_2(x) = \frac{\sigma}{4}\ln[x^2+(b+c)^2] - \frac{\sigma}{4}\ln[x^2+(b-c)^2], \quad (37b)$$

$$g_2(y) = \frac{\sigma}{4}\ln[a^2+(y+c)^2] - \frac{\sigma}{4}\ln[a^2+(y-c)^2], \quad (37c)$$

$$U_2(x) = \frac{\sigma}{2}\left[\frac{(b+c)}{x^2+(b+c)^2} - \frac{(b-c)}{x^2+(b-c)^2}\right]. \quad (37d)$$

These functions are infinitely differentiable and can be presented in form of the Fourier series,

$$V_2(y) = \sum_{n=1}^{\infty}(-1)^n V_n^{(2)}\sin(\gamma_n y),$$
$$V_n^{(2)} = \frac{(-1)^n}{b}\int_{-b}^{b} V_2(y)\sin(\gamma_n y)dy, \quad (38a)$$

$$f_2(x) = \sum_{m=1}^{\infty}(-1)^m f_m^{(2)}\cos(\alpha_m x),$$
$$f_m^{(2)} = \frac{(-1)^m}{a}\int_{-a}^{a} f_2(x)\cos(\alpha_m x)dx, \quad (38b)$$

$$g_2(y) = \sum_{n=1}^{\infty}(-1)^n g_n^{(2)}\sin(\gamma_n y),$$
$$g_n^{(2)} = \frac{(-1)^n}{b}\int_{-b}^{b} g_2(y)\sin(\gamma_n y)dy, \quad (38c)$$

$$U_2(x) = \sum_{m=1}^{\infty}(-1)^m U_m^{(2)}\cos(\alpha_m x),$$
$$U_m^{(2)} = \frac{(-1)^m}{a}\int_{-a}^{a} U_2(x)\cos(\alpha_m x)dx, \quad (38d)$$

where the shorthand notation for α_m and γ_n,

$$\alpha_m = \frac{(2m-1)\pi}{2a} \quad \text{and} \quad \gamma_n = \frac{n\pi}{b}, \quad (39)$$

was introduced.

The leading terms of the Fourier coefficients are

$$V_n^{(2)} = -\frac{2V_2(b)}{b\gamma_n} + \frac{2V_2''(b)}{b\gamma_n^3} - \frac{(-1)^n}{b\gamma_n^4}\int_{-b}^{b} V_2^{(\mathrm{IV})}(y)\times\sin(\gamma_n y)dy, \quad (40a)$$

$$f_m^{(2)} = -\frac{2f_2(a)}{a\alpha_m} + \frac{2f_2''(a)}{a\alpha_m^3} - \frac{2f_2^{(\mathrm{IV})}(a)}{a\alpha_m^5} - \frac{(-1)^m}{a\alpha_m^5}\int_{-a}^{a} f_2^{(\mathrm{V})}(x)\times\sin(\alpha_m x)dx, \quad (40b)$$

$$g_n^{(1)} = -\frac{2g_2(b)}{b\gamma_n} + \frac{2g_2''(b)}{b\gamma_n^3} - \frac{2g_2^{(\mathrm{IV})}(b)}{b\gamma_n^5} + \frac{(-1)^n}{b\gamma_n^5}\int_{-b}^{b} g_2^{(\mathrm{V})}(y)\times\cos(\gamma_n y)dy, \quad (40c)$$

$$U_m^{(2)} = -\frac{2U_2(a)}{a\alpha_m} + \frac{2U_2''(a)}{a\alpha_m^3} + \frac{(-1)^m}{a\alpha_m^4}\int_{-a}^{a} U_2^{(\mathrm{IV})}(x)\times\cos(\alpha_m x)dx. \quad (40d)$$

The parity of these functions, implying that ψ_2 has to be an even function in the x coordinate and an odd function in the y coordinate, leads to (the derivation is rather similar to that of problem 1 and details are therefore omitted)

$$\psi_2(x,y) = b\sum_{m=1}^{\infty}\frac{(-1)^m}{\alpha_m}X_m^{(2)}P_m^{(2)}(y)\cos(\alpha_m x) - a\sum_{n=1}^{\infty}\frac{(-1)^n}{\gamma_n}Y_l^{(2)}Q_n^{(2)}(x)\sin(\gamma_n y) - \sum_{m=1}^{\infty}(-1)^m f_m^{(2)}\frac{\sinh(\alpha_m y)}{\sinh(\alpha_m b)}\cos(\alpha_m x) - \sum_{n=1}^{\infty}(-1)^n g_n^{(2)}\frac{\cosh(\gamma_n x)}{\cosh(\gamma_n a)}\sin(\gamma_n y). \quad (41)$$

Here the odd function $P_m^{(2)}(y)$ and even function $Q_n^{(2)}(x)$ are defined as

$$P_m^{(2)}(y) = b\coth(\alpha_m b)\frac{\sinh(\alpha_m y)}{\sinh(\alpha_m b)} - y\frac{\cosh(\alpha_m y)}{\sinh(\alpha_m b)},$$

$$Q_n^{(2)}(x) = a\tanh(\gamma_n a)\frac{\cosh(\gamma_n x)}{\cosh(\gamma_n a)} - x\frac{\sinh(\gamma_n x)}{\cosh(\gamma_n a)}. \tag{42}$$

The expansion coefficients $X_m^{(2)}$ and $Y_n^{(2)}$ are specified by the following coupled infinite series:

$$X_m^{(2)} b\Delta_2(\alpha_m b) - \sum_{n=1}^{\infty} Y_n^{(2)} \frac{4\alpha_m^2\gamma_n}{(\alpha_m^2+\gamma_n^2)^2} = H_m^{(2)}, \quad m = 1,2,\ldots, \tag{43a}$$

$$Y_n^{(2)} a\Delta_1(\gamma_n a) - \sum_{m=1}^{\infty} X_m^{(2)} \frac{4\gamma_n^2\alpha_m}{(\gamma_n^2+\alpha_m^2)^2} = I_n^{(2)}, \quad n = 1,2,\ldots. \tag{43b}$$

Within this formulation, the shorthand notation $\Delta_2(\xi)$ stands for

$$\Delta_2(\xi) = \coth(\xi) - \frac{\xi}{\sinh^2\xi}, \tag{44}$$

while the definition of $\Delta_1(\xi)$ is given by (17).

The free terms $H_m^{(2)}$ and $I_n^{(2)}$ are given by

$$H_m^{(2)} = \alpha_m^2\left(\frac{2}{a}\sum_{n=1}^{\infty} g_n^{(2)}\frac{\gamma_n}{\alpha_m^2+\gamma_n^2} - f_m^{(2)}\coth(\alpha_m b) + \frac{U_m^{(2)}}{\alpha_m}\right), \tag{45}$$

$$I_n^{(2)} = -\gamma_n^2\left(\frac{2}{b}\sum_{m=1}^{\infty} f_m^{(2)}\frac{\alpha_m}{\gamma_n^2+\alpha_m^2} - g_n^{(2)}\tanh(\gamma_n a) + \frac{V_n^{(2)}}{\gamma_n}\right). \tag{46}$$

As in the previous problem, the free terms may be expressed in an integral form, by which their asymptotic behavior for large indices becomes clear,

$$H_m^{(2)} = \frac{(-1)^m}{a\alpha_m^3}\int_{-a}^{a}[U_2^{(\mathrm{IV})}(x)\cos(\alpha_m x) + f_2^{(\mathrm{V})}(x) \times\coth(\alpha_m b)\sin(\alpha_m x)]dx + \frac{1}{a\alpha_m^3}\int_{-b}^{b} g_2^{(\mathrm{V})}(y) \times\frac{\cosh(\alpha_m y)}{\sinh(\alpha_m b)}dy = \mathcal{O}(m^{-4}), \quad m\to\infty, \tag{47}$$

$$I_n^{(2)} = -\frac{(-1)^n}{b\gamma_n^3}\int_{-b}^{b}[V_2^{(\mathrm{IV})}(y)\sin(\gamma_n y) - g_2^{(\mathrm{V})}(y) \times\tanh(\gamma_n b)\cos(\gamma_n y)]dy - \frac{1}{b\gamma_n^3}\int_{-a}^{a} f_2^{(\mathrm{V})}(x) \times\frac{\sinh(\gamma_n x)}{\cosh(\gamma_n a)}dx = \mathcal{O}(n^{-4}), \quad n\to\infty. \tag{48}$$

In a similar way, the asymptotic behavior of the coefficients with large numbers of indices is

$$X_m^{(2)} = \frac{E_2}{\alpha_m} + \mathrm{Re}\left(\frac{E_2^{(\gamma)}}{\alpha_m^{\gamma}}\right), \quad m\to\infty,$$

$$Y_n^{(2)} = \frac{E_2}{\gamma_n} - \mathrm{Re}\left(\frac{E_2^{(\gamma)}}{\gamma_l^{\gamma}}\right), \quad n\to\infty, \tag{49}$$

where $\gamma = 2.739593 + i1.119025$, as in problem 1, and $E_2^{(\gamma)}$ is some complex-valued constant. The real-valued constant E_2 is given by

$$\frac{\pi}{2ab}E_2 = \sum_{m=1}^{\infty} H_m^{(2)} + \sum_{n=1}^{\infty} I_n^{(2)} = 0. \tag{50}$$

(Here the algebra becomes even more sophisticated than in problem 1, although the final result is the same.)

The final representation for the stream function Ψ_2 reads

$$\begin{aligned}\Psi_2(x,y) = {} & b\sum_{m=1}^{\infty}\frac{(-1)^m}{\alpha_m}X_m^{(2)}P_m^{(2)}(y)\cos(\alpha_m x) \\ & - a\sum_{n=1}^{\infty}\frac{(-1)^n}{\gamma_n}Y_n^{(2)}Q_n^{(2)}(x)\sin(\gamma_l y) \\ & - \sum_{m=1}^{\infty}(-1)^m\bar{f}_m^{(2)}\frac{\sinh(\alpha_m y)}{\sinh(\alpha_m b)}\cos(\alpha_m x) \\ & - \sum_{n=1}^{\infty}(-1)^n\bar{g}_n^{(2)}\frac{\cosh(\gamma_n x)}{\cosh(\gamma_n a)}\sin(\gamma_n y) - C_2\frac{y}{b} \\ & + D_2\frac{y}{6b}[3(a^2-x^2)-(b^2-y^2)] \\ & + \frac{\sigma}{4}\ln[x^2+(y+c)^2] - \frac{\sigma}{4}\ln[x^2+(y-c)^2].\end{aligned} \tag{51}$$

The constants C_2 and D_2 are given by

$$C_2 = f_2(a) = g_2(b) = \frac{\sigma}{4}\ln[a^2+(b+c)^2] - \frac{\sigma}{4}\ln[a^2+(b-c)^2]$$

and

$$D_2 = f_2''(a) = -g_2''(b) = -\frac{\sigma}{2}\left[\frac{a^2-(b+c)^2}{[a^2+(b+c)^2]^2} - \frac{a^2-(b-c)^2}{[a^2+(b-c)^2]^2}\right].$$

To obtain the representation (51), we had to introduce new Fourier coefficients $\bar{f}_m^{(2)}$ and $\bar{g}_n^{(2)}$ [which follow directly from (40b) and (40c)],

TABLE II. Numerical values of the first eight free terms and expansion coefficients of problem 1 for the case in which $a=1$, $b=4$, and $c=2.256772$. Once again, any value of c could be used for this purpose, provided $|c|<4$. However, the particular choice of c here is related with a few applications; see Sec. IV.

m,n	$H_m^{(2)}$	$I_n^{(2)}$	$-\alpha_m \bar{f}_m^{(2)}$	$\gamma_n \bar{g}_n^{(2)}$	$X_m^{(2)}$	$Y_n^{(2)}$
0	—	—	—	0.2870743	—	—
1	0.3189331	−0.4562471	0.1027773	−0.3178814	-2.5750×10^{-3}	−0.4144911
2	-4.0064748×10^{-3}	−0.1929772	3.6103397×10^{-3}	-5.3351480×10^{-2}	-2.8970×10^{-3}	−0.1669958
3	2.7937793×10^{-5}	0.2859568	1.5880261×10^{-3}	6.6177047×10^{-2}	5.029×10^{-4}	0.2667589
4	-1.6364437×10^{-7}	0.1536788	8.2441856×10^{-4}	2.27275212×10^{-2}	3.498×10^{-4}	0.1492170
5	8.8029144×10^{-10}	-6.4786355×10^{-2}	5.0213684×10^{-4}	-6.5003510×10^{-3}	2.072×10^{-4}	-6.57512×10^{-2}
6	-4.5015035×10^{-12}	-6.2210062×10^{-2}	3.3724385×10^{-4}	-5.3989318×10^{-3}	1.259×10^{-4}	-6.32539×10^{-2}
7	2.2258153×10^{-14}	5.6043915×10^{-3}	2.4190134×10^{-4}	1.3845507×10^{-3}	7.98×10^{-5}	4.6328×10^{-3}
8	-1.0745049×10^{-16}	1.8414175×10^{-2}	1.8190027×10^{-4}	2.1300894×10^{-3}	5.25×10^{-5}	1.75812×10^{-2}

$$\bar{f}_m^{(2)} = f_m^{(2)} + \frac{2f_2(a)}{a\alpha_m} - \frac{2f_2''(a)}{a\alpha_m^3} = -\frac{2f_2^{(\mathrm{IV})}(a)}{a\alpha_m^5} - \frac{(-1)^m}{a\alpha_m^5} \times \int_{-a}^{a} f_2^{(\mathrm{V})}(x)\sin(\alpha_m x)dx = \mathcal{O}(m^{-4}), \quad m\to\infty \tag{52}$$

and

$$\bar{g}_n^{(2)} = g_n^{(2)} + \frac{2g_2(b)}{b\gamma_n} - \frac{2g_2''(b)}{b\gamma_n^3} = -\frac{2g_n^{(\mathrm{IV})}(b)}{b\gamma_n^5} - \frac{(-1)^n}{b\gamma_n^5} \times \int_{-b}^{b} g_2^{(\mathrm{V})}(y)\cos(\gamma_n y)dy = \mathcal{O}(n^{-4}), \quad n\to\infty. \tag{53}$$

Besides that, we applied the following relations:

$$\frac{2}{a}\sum_{m=1}^{\infty}\frac{(-1)^m}{\alpha_m}\frac{\sinh(\alpha_m y)}{\sinh(\alpha_m b)}\cos(\alpha_m x) + \frac{2}{b}\sum_{n=1}^{\infty}\frac{(-1)^n}{\gamma_n}\frac{\cosh(\gamma_n x)}{\cosh(\gamma_n a)}\sin(\gamma_n y) = -\frac{y}{b}, \tag{54}$$

and

$$\frac{2}{a}\sum_{m=1}^{\infty}\frac{(-1)^m}{\alpha_m^3}\frac{\sinh(\alpha_m y)}{\sinh(\alpha_m b)}\cos(\alpha_m x) - \frac{2}{b}\sum_{n=1}^{\infty}\frac{(-1)^n}{\gamma_n^3}\frac{\cosh(\gamma_n x)}{\cosh(\gamma_n a)}\sin(\gamma_n y) = -\frac{y}{6b}[3(a^2-x^2)-(b^2-y^2)]. \tag{55}$$

Table II displays the first eight values of the expansion coefficients and the free terms for the second elemental problem under the same conditions as used for Table I, thus with $a=1$, $b=4$, and $c=2.256772$. The given free terms $H_m^{(2)}$ and $I_n^{(2)}$ and the Fourier coefficients $-\alpha_m \bar{f}_m^{(2)}$, $\gamma_n \bar{g}_n^{(2)}$ have a relative numerical error of 10^{-7}. The expansion coefficients $X_m^{(2)}$ and $Y_n^{(2)}$ are determined with an absolute error of 10^{-7}.

At this point, all the information is acquired to calculate the overall stream function $\Psi(x,y)$ of the full problem by summing the results for the elemental stream functions $\Psi_1(x,y)$ and $\Psi_2(x,y)$.

III. MULTICELLULAR FLOW PATTERNS IN A SLENDER CAVITY

Due to the viscosity of the fluid, the walls, and therefore the geometry of the cavity, have a significant part in the development of the final flow structure. For rectangular cavities, for instance, multicellular Stokes flows are observed in narrow, elongated geometries, despite the exact nature of the driving mechanism. In this section, two types of internally stirred cavity flows will be examined on their characteristic properties. In the first case, the creeping cavity flow is induced by a single rotlet, whereas in the second case two symmetrically placed—either corotating or counterrotating—rotlets are applied to generate the fluid motion. Actually, the latter case is identical to the elemental flow problems 1 and 2, as described in the preceding section.

Of special interest is the role of the geometry of the cavity, and in particular in what way the flow will be affected by a change in the cavity's aspect ratio. It is known that in this respect the corner points are of significant importance. By setting the value of the rotlet position c equal to zero, the elemental stream function Ψ_1 now represents a cavity flow induced by a single rotlet of intensity σ, as may easily be seen from Fig. 1 by putting the imaginary rotlets of problem 1 at the center of the cavity. Because the rotlets of problem 2 rotate in opposite directions, their individual contributions will be canceled out. Note that this is only true for the center position; for all other positions, both Ψ_1 and Ψ_2 have to be calculated individually and added up in order to obtain the overall flow description. The same result may be obtained formally by putting $c=0$ in the expressions derived for Ψ_1 and Ψ_2 in the previous section. Figure 2 displays some typical streamline portraits for different values of the domain aspect ratio A. The streamline patterns show an increase of the number of cells for increasing aspect ratio. It is clear that the flow field shown in Fig. 2(b), containing two hyperbolic

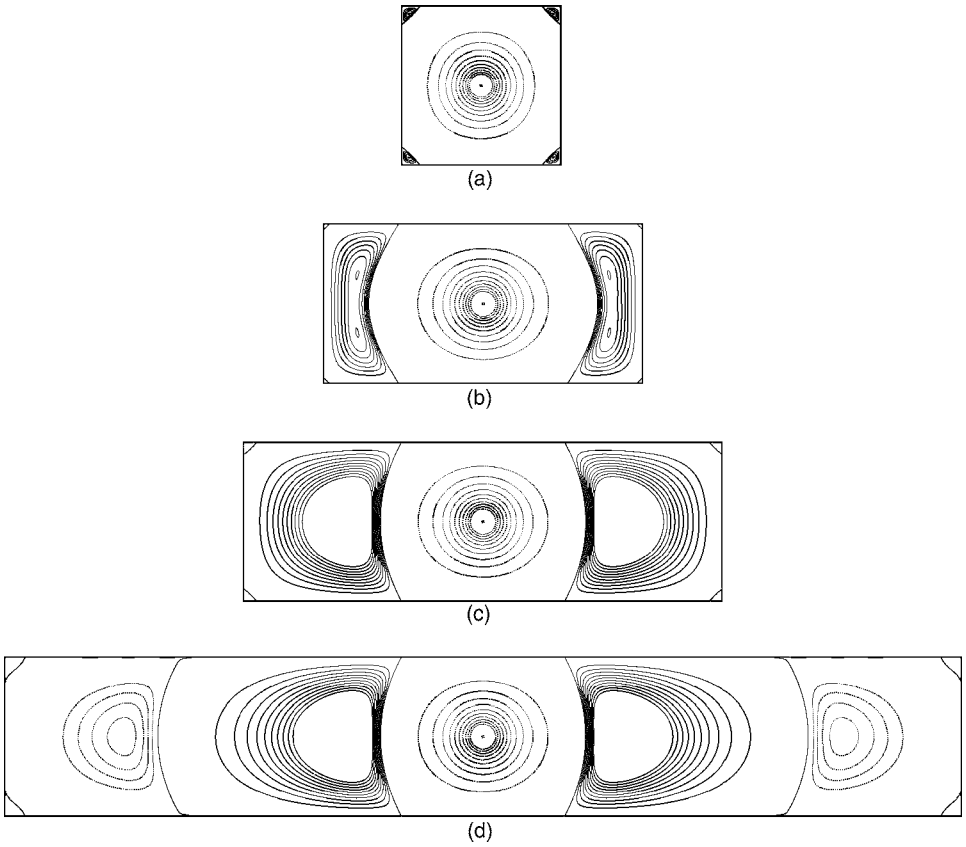

FIG. 2. Stream function contour plots of the Stokes flow due to a single rotlet, positioned in the origin of the domain, $c=0$ with (a) $A=1$, (b) $A=2$, (c) $A=3$, (d) $A=6$. Dashed contours represent negative values of the stream function, and solid contours represent positive values. The contour level increment is 0.15 for the dashed lines of the central cell; 0.005 for the solid lines in (b); 0.001 for the solid lines in frames (c) and (d); and 1×10^{-5} for the dashed lines of the outer cells in frame (d). For the corner cells of frame (a), the contour increment is 2×10^{-5}.

points, can be considered as an intermediate state with the single central cell shown in Fig.2(a) and the multicellular pattern of Fig. 2(c).

A comparison between Figs. 2(c) and 2(d) shows that—while gradually increasing the aspect ratio—once the single-core cells have been formed, their size and their position within the cavity remain more or less unchanged. For the central cell, this is clearly seen in Figs. 2(b)–2(d). The same holds for the secondary single-core cells and it is expected that it is also true for additional cells formed in increasingly slender cavities. So, once the cells have reached their final size, new additional cells can only be formed when extra space is added to the cavity, thus by elongating the cavity to larger aspect ratios.

Figure 2(a) shows further the presence of small corner cells; these corner eddies can also be observed for the other aspect ratios when one would zoom in (here, only the dividing $\Psi=0$ streamlines were plotted).

For the situation of Figs. 2(a) and 2(c), we have plotted in Fig. 3 the isovorticity lines. Figure 4 displays the corresponding ω, Ψ scatter-plots showing that there is no functional relation between the vorticity and the stream function since the isovorticity lines and iso-Ψ lines display different patterns and do not coincide. Apparently, the Jacobian between the vorticity and the stream function does not have to be zero for the stationary, highly viscous flow where the Reynolds number has been set identically to zero. The absence of a one-to-one correspondence between these quantities was also reported by Van de Konijnenberg, Flór, and van Heijst[33] in their study on the decay of bounded quasi-two-dimensional viscous flows. In the origin of the domain, where the rotlet is positioned, the vorticity is determined by the rotlet circulation $\Gamma^{(\sigma)}=2\pi\sigma$ around a closed contour enclosing the rotlet.

An important issue concerns the question of how the existence of a multicellular structure in slender cavities can be explained. Hellou and Coutanceau[21] demonstrated in a rather detailed experimental and numerical study on a cellular Stokes flow induced by a rotating cylinder how the formation process of a new single cell starts from the corners.

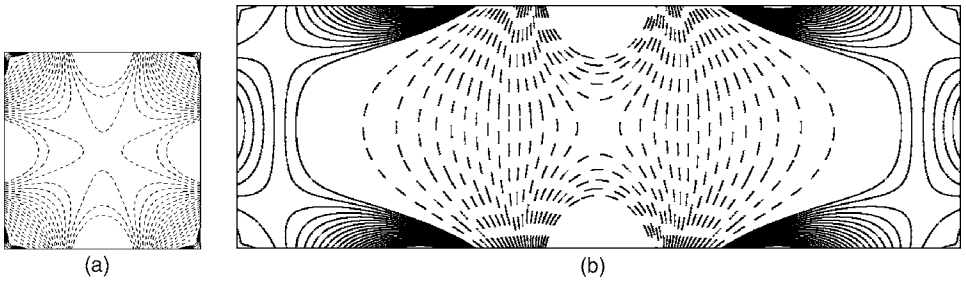

FIG. 3. Contour plot of the vorticity (ω) for aspect ratio $A=1$ (a) and $A=3$ (b). Dashed contours represents negative values of the vorticity, and solid contours represent positive values. The contour level increment is 0.1 for the dashed lines and 0.01 for the solid lines.

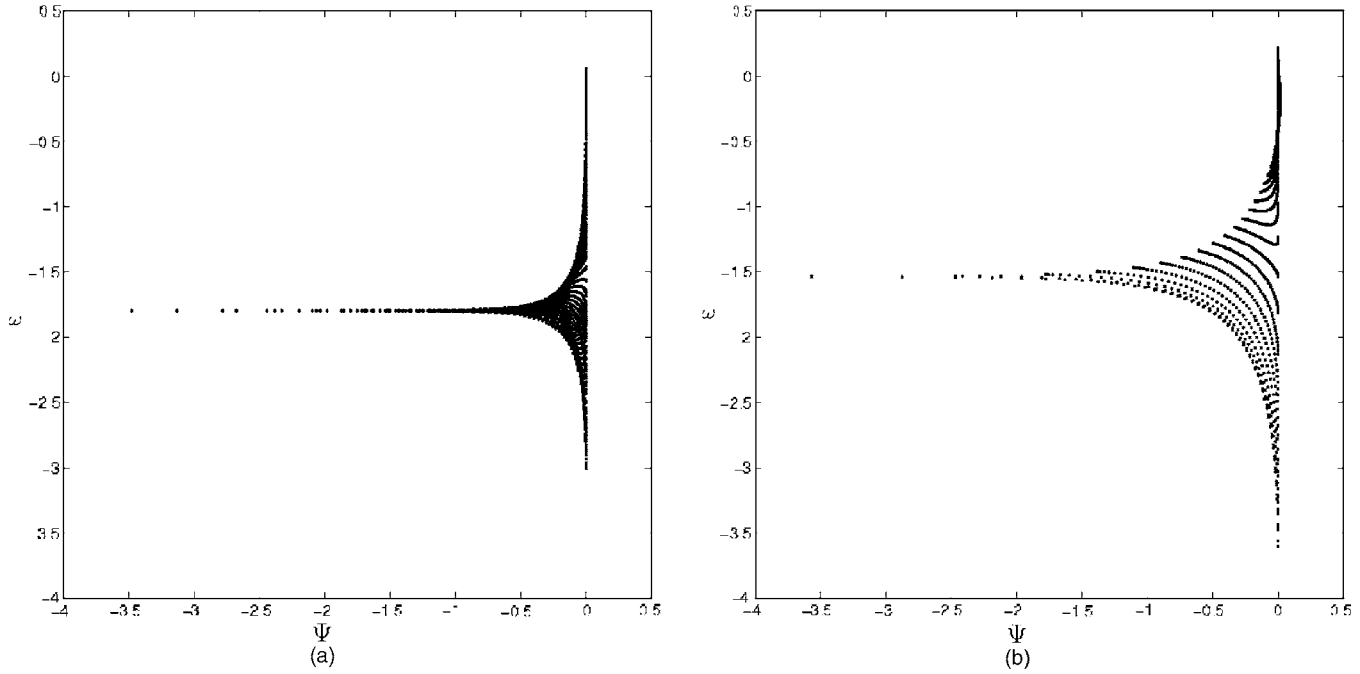

FIG. 4. The scatter-plot shows that there is no functional relation between ω and Ψ. (a) $A=1$, (b) $A=3$.

By increasing the value of the aspect ratio A gradually, numerical and experimental results show how two main corner cells grow in size until they come into contact by means of a saddle point, to finally merge and give rise to the formation of a new, single-core cell. If the aspect ratio is increased further, more new cells will be formed, which ultimately leads to a large number of cells. The multicellular flow structure in the present case of a single rotlet in a slender, rectangular cavity can be explained in the same way as for the cylinder-driven flow considered by Hellou and Coutanceau,[21] as is demonstrated in Fig. 5. The main difference is that the first additional cell will be formed at a larger aspect ratio, but all the essential features of the merging process are present. In Figs. 5(e)–5(g), the presence of new corner cells can already be observed. The evolution of the axial stagnation point of the first secondary cell during the process of coalescing is shown in Fig. 6. Comparison with the cylinder-driven flow shows a similar development, in which the stagnation point reaches a minimum at the stage at which the corner cells have just been merged fully and the hyperbolic stagnation point has become an elliptic point ($A \approx 2.08$). Further increase of the aspect ratio shows that the stagnation point reaches (asymptotically) a fixed position, independent of further increment of A.

The flow structures of the elemental stream functions Ψ_1 and Ψ_2 (with $c_0 \neq 0$) are displayed in Fig. 7 for two different values of the aspect ratio and three values of the rotlet position: $A=4/3$ and $c_0=0.71361$; $A=4$ and $c_0=0.86097$; and $A=4$ and $c_0=2.2568$. The resemblance with the Stokes flow inside a rectangular domain of which the flow is completely

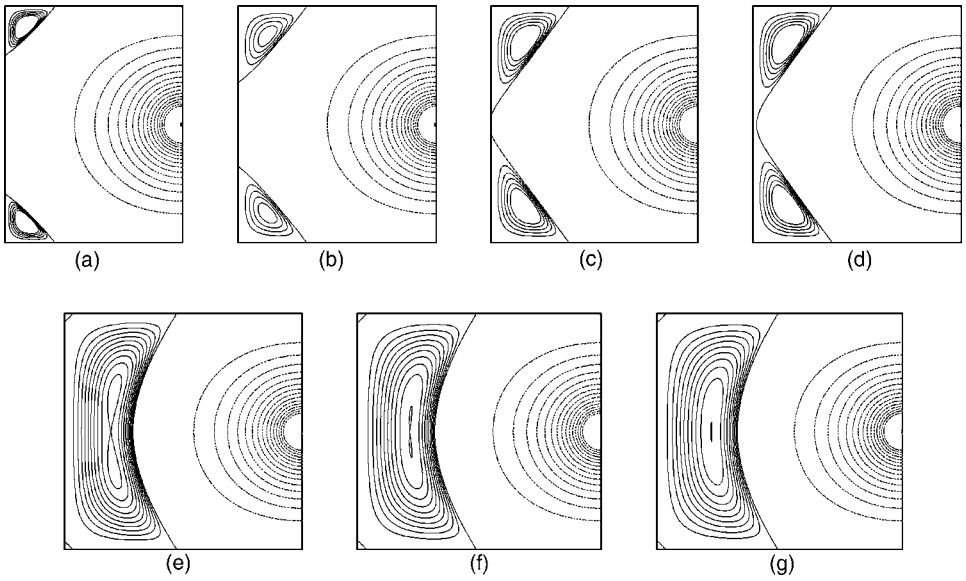

FIG. 5. Formation of the first secondary cell from the corner cells: (a) $A=1.50$, $\Delta\Psi_c=2\times10^{-5}$; (b) $A=1.68$, $\Delta\Psi_c=1\times10^{-4}$; (c) $A=1.75$, $\Delta\Psi_c=1\times10^{-4}$; (d) $A=1.76$, $\Delta\Psi_c=1\times10^{-4}$; (e) $A=2.01$, $\Delta\Psi_c=3.569\times10^{-4}$; (f) $A=2.06$, $\Delta\Psi_c=4.8605\times10^{-4}$; (g) $A=2.08$, $\Delta\Psi_c=5.39\times10^{-4}$. Here, $\Delta\Psi_c$ denotes the contour increment of the corner cells. The dashed contours of the central cell have negative values; the increment is 0.01.

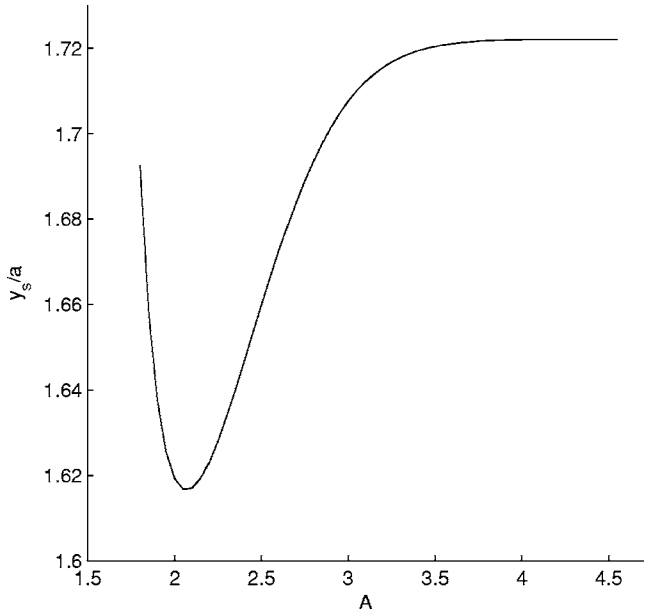

FIG. 6. Evolution of the position of the axial stagnation point during the formation process of the first secondary cell.

determined by the externally assigned tangentially moving top and bottom wall, as described by Jana, Metcalfe, and Ottino,[22] is evident. In order to make a more direct comparison, the same aspect ratios were taken as those used in Fig. 4 of Ref. 22. Globally, we recognize the same flow structure for both forcing methods. For $A=1.33$, the Ψ_1 structure of Fig. 7(a) corresponds to Fig. 4(a) of Ref. 22, in which the walls move in opposite directions: both figures show the hyperbolic stagnation point at the origin of the domain. Two elliptic stagnation points are found in the flows of Ψ_2 [Fig. 7(a)] and that induced by the comoving walls of Fig. 4(b) of Ref. 22. Similar remarks can be made for the flow cells inside the cavity with $A=4$ provided the rotlets are placed relatively close to the top and bottom wall [compare Fig. 7(c) with Figs. 4(c) and 4(d) of Ref. 22]. For this value of the aspect ratio and rotlet position, the secondary cells are now the ones in the central part of the domain, since they are induced by the primary cells at the short side of the domain. When, on the other hand, the rotlets are placed near the origin of the domain, that is, if $c_0=0.86097$, the central cells are the primary ones. As a result, the flow pattern is different. Although there is a global resemblance between the two cavity flows, the fact that forcing mechanisms are different (externally versus internally driven cavity flow) is responsible for the fact that the primary cells in the externally driven flow are much more flattened than those of the rotlet-induced flow (the no-slip boundary condition of the moving walls is obviously the reason for that). But a more striking difference is probably that the corner eddies of Fig. 7(c) have a relatively large size compared to the driven-cavity case.[22]

The positions of the rotlets in Fig. 7 are not chosen arbitrarily. The solution shows that for a certain position of the rotlet $(0,c_0)$, the flow has a stagnation point $(0,-c_0)$ symmetrically placed inside the rectangle. This means that the rotlets do not influence each other's flow field. It goes without saying that for practical application this is of great importance. Moreover, it turns out that for narrow cavity geometries, several of these special rotlet positions can be found.

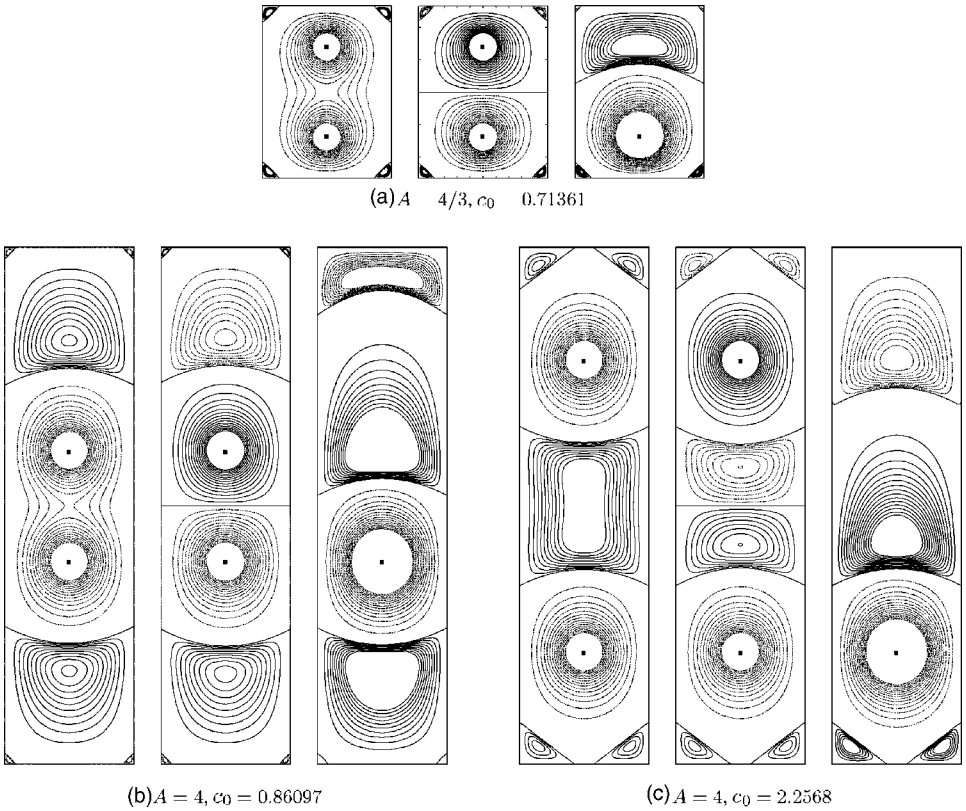

FIG. 7. From the left to the right: isolines of Ψ_1, Ψ_2, and $\Psi=\Psi_1+\Psi_2$ for different rotlet positions and two values of the aspect ratio. Dashed contours represent negative values of the stream function, and solid contours represent positive values. For all plots, it holds that the contour level increment is 0.03 for the main cells and 0.001 for the secondary cells. The contour increment in the $\Psi_{1,2}$ plots of the corner cells is 5×10^{-8} (b) and 1×10^{-4} (c). For the Ψ plots we used in addition $\Delta\Psi=0.0001$ for the corner cells (a), $\Delta\Psi=2\times10^{-7}$ for the corner cells (b), and $\Delta\Psi=0.0001$ for the (bottom) corner cells and $\Delta\Psi=5\times10^{-6}$ for the top cell (c).

TABLE III. Rotlet positions $(x,y)=(0,c_0)$ producing symmetrically located stagnation points $(0,-c_0)$ for various values of the aspect ratio A.

A	$c_0^{(1)}$	$c_0^{(2)}$	$c_0^{(3)}$	$c_0^{(4)}$
1	0.54328	—	—	—
2	0.84694	—	—	—
3	0.86076	2.19566	—	—
4	0.86097	2.25677	3.4491	—
5	0.86098	2.25791	3.6477	—
6	0.86098	2.25793	3.6537	5.02045

In Table III, the values of c_0 are listed for some different aspect ratios.

It is important to notice that for slender cavities (large aspect ratios), the exact location of these special rotlet positions does not depend, at least not strongly, upon the value of the aspect ratio. For those situations, the flanking single-core cells have reached their final size and position, and a further increase of A does not change that anymore.

IV. CHAOTIC TRANSPORT IN A BOUNDED STOKES FLOW

In a second application, a time-dependent Stokes flow is considered. Time-dependency of a two-dimensional flow may give rise to chaotic advection of passive tracer particles released somewhere in the fluid. The flow is generated by two individually adjustable rotlets, which will be denoted by α and β. The rotlet forcing is made time-dependent in two ways. First, the rotlets are switched "on" and "off" periodically, which is known as the blinking rotlet model. It was used before by Meleshko and Aref[1] in a study on chaotic transport in a circular domain. Secondly, the forcing is made time-dependent by changing the strength of the rotlets in time sinusoidally. Besides the question of how these two different time-dependent forcing protocols affect the stirring properties of the flow, also the influence of the phase difference between the individual rotlets upon the stirring quality is taken into account.

The two rotlets α and β are positioned at $(0,c_0)$ and $(0,-c_0)$, respectively, for which the rotlet position and stagnation point are indeed symmetrically located. With Ψ_α and Ψ_β denoting the stream functions associated with the flows generated by the individual rotlets α and β, the time-dependent stream function Ψ is assumed to be given in a quasistationary form

$$\Psi(x,y,t)=\lambda_\alpha(t)\Psi_\alpha(x,y)+\lambda_\beta(t)\Psi_\beta(x,y). \tag{56}$$

The time-independent contributions Ψ_α and Ψ_β are directly related to the elemental stream functions $\Psi_{1,2}$ through

$$\begin{aligned}\Psi_\alpha(x,y;c_0)&=\Psi_1(x,y;c_0)-\Psi_2(x,y;c_0),\\ \Psi_\beta(x,y;-c_0)&=\Psi_1(x,y;c_0)+\Psi_2(x,y;c_0).\end{aligned} \tag{57}$$

In principle, the functions $\lambda_{\alpha,\beta}$ may be any function in time. What matters is that it is assumed that whenever a rotlet is switched "on," the impact on the surrounding fluid is instantaneously present in the entire domain. In general, this is obviously not true, but under certain conditions a quasistationary approach to the problem is justified; and if that is the case, then the time-independent stream functions $\Psi_{\alpha,\beta}$ are given by the expressions derived in Sec. II.

Three different time scales can be introduced: the momentum diffusion time scale $\tau_d=L^2/\nu$, the advection time scale $\tau_a=L/U$ as the characteristic time of the tracer dynamics, and the forcing period T. Here, L and U are typical length and velocity scales, respectively. A natural choice for L is the container width, and the typical velocity scale U should be related with the rotlet intensity σ, i.e., the best choice is $U=\sigma/L$. Two dimensionless numbers can be constructed: the forcing Strouhal number, $\mathrm{Sr}_f=\tau_d/T$, and the ratio $D=T/\tau_a=UT/L=\sigma T/L^2$. The latter quantity is a measure for the dimensionless displacement of a tracer particle during one forcing period. The assumption of quasistationarity requires $\mathrm{Sr}_f\ll 1$, which translates into $\sigma\ll D\nu$ or $\tau_a\gg\tau_d/D$. If this condition is not satisfied, the fluid cannot respond in time to the changes in forcing strength, and a solution based upon the time-dependent equation of motion has to be taken into account. In what follows, we assume that $\mathrm{Sr}_f\ll 1$.

In order to reveal the transport properties of this rotlet-driven cavity flow, the deformation of a passive material blob is monitored in time. Computationally, it is sufficient to consider just the deformation of the enclosing contour C. The contour is defined by markers connected by small linear line segments. The number of marker points is chosen such that the contour appears to be smooth. During the evolution of the flow, the contour may be deformed considerably by successive stretching and folding, which can lead to a significant increase of the contact length with the surrounding fluid. As time progresses, new (deformed) contours are calculated by integrating the equation of motion numerically for each individual marker. The integration is performed by an extrapolation algorithm, based on an explicit midpoint rule with variable order and variable step size.[27] In order to maintain the smoothness of the initial contour, it might be necessary to insert new marker points on the contour. These new points are added when the distance between neighboring markers exceeds a certain prescribed threshold value, or when the angle between neighboring line segments becomes less than 120°. These points are placed on the initial contour after which the time integration for the new markers starts from the beginning until the present time has been reached and a new calculation is continued for the entire collection of markers. Instead of adding marker points, markers are removed when the length of a connecting line segment becomes so small that computation time can be saved without loss of noticeable smoothness or accuracy. Due to incompressibility of the flow, the area S enclosed by the contour C has to be conserved after each time step. The area is calculated numerically each time step by applying Stokes' theorem,

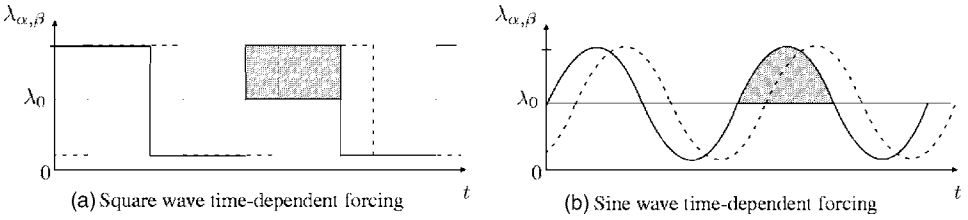

FIG. 8. Time-dependent fluid forcing by two rotating rotlets α (solid line) and β (dashed line).

$$S = \int\int_S dxdy = \frac{1}{2}\oint_C (xdy - ydx) \approx \frac{1}{2}\sum_{m=1}^{M} (x_m y_{m+1} - y_m x_{m+1}), \tag{58}$$

with M the number of markers defining contour C, and provides an instrument to check the accuracy of the advection calculations. In the numerical calculation performed in this section, the area is preserved with a relative error less than 1×10^{-3}. A more detailed description of this contour-kinematic method can be found in Meleshko and Van Heijst.[34]

As mentioned before, in the blinking rotlet model, the rotlets are switched "on" and "off" periodically and so the time-dependent functions λ_α and λ_β are periodic square waves, which in general may be written as

$$\lambda_\alpha(t) = \begin{cases} (\lambda_0 + A_0), & \text{for } nT \leq t < \left(n+\frac{1}{2}\right)T, \\ (\lambda_0 - A_0), & \text{for } \left(n+\frac{1}{2}\right)T \leq t < (n+1)T; \end{cases} \tag{59}$$

$$\lambda_\beta(t) = \begin{cases} (\lambda_0 + A_0), & \text{for } (n+k_\beta)T \leq t < \left(n+k_\beta+\frac{1}{2}\right)T, \\ (\lambda_0 - A_0), & \text{for } \left(n+k_\beta+\frac{1}{2}\right)T \leq t < (n+k_\beta+1)T. \end{cases} \tag{60}$$

Here, λ_0 is the average forcing, A_0 is the forcing amplitude, and k_β is the phase at which rotlet β is switched "on" for the first time; T is the full blinking period and $n=0,1,2,\ldots$.

In the situation in which the fluid is forced to motion by a sine wave time-dependent forcing protocol, the functions $\lambda_{\alpha,\beta}$ read

$$\lambda_\alpha(t) = \lambda_0 + A\sin\frac{2\pi t}{T}, \tag{61}$$

$$\lambda_\beta(t) = \lambda_0 + A\sin 2\pi\left(\frac{t}{T} + k_\beta\right). \tag{62}$$

Here A is the amplitude of the sinusoidal forcing. The protocols, which are displayed graphically in Fig. 8, are studied upon their stirring quality, varying the phase difference between the rotlets activity. The forcing amplitudes are chosen such that the shaded areas under the curves in Fig. 8, which is a measure for the forcing quality, are in both cases the same for a given average forcing λ_0. In addition, we impose the restriction $A_0, A \leq \lambda_0$.

The influence of the aspect ratio is considered only for the blinking rotlet scenario. But first a comparison is made between the transport properties of a blinking rotlet flow inside a square cavity (with $k_\beta=1/2$) and a circular cavity, which was the original geometry in which the blinking rotlet model was first applied to study transport properties of a confined Stokes flow.[1] Figure 2 of Meleshko and Aref[1] displays the deformation of an initially circular passive blob of radius $r_0=0.1a$, centered between two blinking rotlets with strength $\sigma=1.17a^2/T$ (or $D=1.17$) after several blinking periods. Here a and T were the radius of the domain and the blinking period, respectively. Each rotlet was placed symmetrically in the stagnation point of the other, i.e., in $(r,\theta)=(c_0,0)$ and $(r,\theta)=(c_0,\pi)$, with $c_0=a[(\sqrt{17}-3)/4]^{1/2}\approx 0.53a$,[1] and with r and θ the plane polar coordinates with respect to the domain center. It is noted here that the tracer evolution is based upon the given closed form of the stream function [Ref. 1, formula (11)], i.e.,

$$\psi(r,\theta) = \frac{\sigma}{2}\left[\ln\frac{r^2 - 2c_0 r\cos\theta + c_0^2}{a^2 - 2c_0 r\cos\theta + c_0^2 r^2/a^2} + \frac{(1-r^2/a^2)(a^2 - c_0^2 r^2/a^2)}{a^2 - 2c_0 r\cos\theta + c_0^2 r^2/a^2}\right] \tag{63}$$

is only correctly reproduced by doubling of the rotlet strength, i.e., if $\sigma=2.34a^2/T$ instead of $\sigma=1.17a^2/T$.

The separate plots of Fig. 9 reveal a strong resemblance with the tracer distribution for the circular geometry as studied by Meleshko and Aref.[1] The distribution plots are not exactly identical, however, as can be seen by comparing Fig.

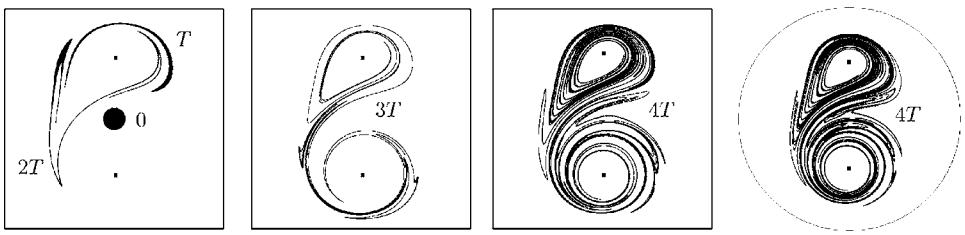

FIG. 9. Stirring of an initially circular blob (initial position indicated by the black circular area in the first plot) due to two blinking rotlets (indicated by dots) after several periods of time.

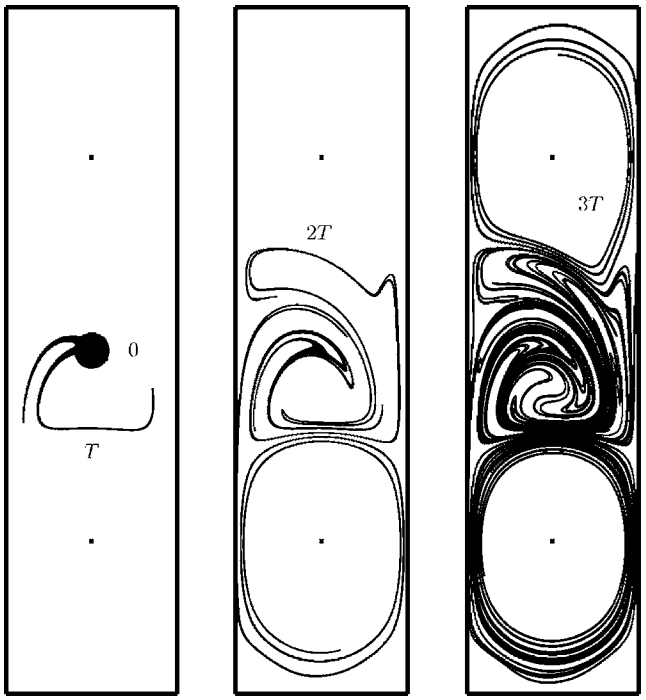

FIG. 10. Evolution of the distribution patterns of an initially circular blob in a rectangular domain with aspect ratio $A=4$; $\sigma=11.76b^2/T$, $c_0=2.25677$, $r_0=0.2a$. The position of the rotlets is indicated by dots. For the blinking rotlet model, we used $k_\beta=1/2$.

9(c) with Fig. 9(d) in which the tracer distribution in the circular domain at $t=4T$ is shown. The qualitative behavior of the flow, however, is quite similar. Apparently, the influence that a difference in domain geometry could have is not strongly apparent for the square domain.

The results of Sec. III demonstrated that the Stokes flow inside a rectangular domain becomes more complex by the appearance of a multicellular pattern when the aspect ratio of the domain is increased. A question that arises immediately is, how do these arrays of flow cells influence the stirring properties of the system? To answer this question qualitatively, the evolution in time of a blob of tracer material is followed numerically. For illustrative purposes, we briefly discuss here the results of numerical experiments for containers with an aspect ratio of 4. The streamline patterns displayed in Figs. 7(a) and 7(b) show that in the center part of the domain, the flows are more or less comparable for containers with aspect ratio $A=4/3$ and 4. The release of a blob of passive tracer in the center of the container with an aspect ratio of 4 would thus give similar results as shown in Fig. 9 for the square container [which would have a stream function pattern similar to the one shown in Fig. 7(a)], at least for short times. Long-time computations might eventually show filaments of tracer in the outer parts of the container. Only when the rotlets are put in the outer stagnation points, see Fig. 7(c), does a clear difference become noticeable between this flow structure and the one displayed in Fig. 7(b), and similar remarks can be made for the tracer distribution. In Fig. 10, the distribution evolution of a blob of passive tracer with an initial radius $r_0=0.2a$, advected due to a blinking rotlet pair (with $k_\beta=1/2$), is presented in the case in which the aspect ratio is 4.

The way in which the passive tracer blob has been advected in time reveals, to a certain degree, the structure of the Ψ_1 function with its top and bottom cell and a rectangularly shaped central cell [see Fig. 7(c)]. In both situations, the rotlets have the same intensity and direction of rotation. The time-dependent nature of the flow allows the tracer blob to intrude in all three regions.

We will now consider the effect of the phase difference k_β on the advection properties. Let the functions $\lambda_{\alpha,\beta}$ have a square-wave time dependency (blinking rotlet model). The effect the phase difference may have upon the stirring quality of the flow is studied by doubling the value of k_β in two consecutive steps, starting at $k_\beta=1/12$, and the results are compared with the traditional blinking rotlet model, i.e., $k_\beta=1/2$. Figure 11 displays the result of the tracer distribution inside a square domain after several blinking periods.

It is clear that when the rotlets are almost simultaneously active ($k_\beta=1/12$), the initially circular blob is stretched out rapidly around the rotlets. But by no means are the tracer particles distributed into a large area of the cavity's interior. By increasing the phase difference in two steps by a factor 2 ($k_\beta=1/6$ and $1/3$), the structure of the tracer contour changes by which the tracer particles can be found in a larger part of the cavity. The situation in which the activity of the rotlets is out of phase ($k_\beta=1/2$) seems to be the most appropriate choice for optimal stirring. This situation was also considered in the comparison between a square domain and a circular domain. In the blinking rotlet model, the functions $\lambda_{\alpha,\beta}$ are itself quasi-time-dependent. In that respect, we take $\lambda_{\alpha,\beta}$ to have a sinusoidal time dependency [see (61)] and study the effect it has upon the stirring quality of the flow. For this comparison, we take $k_\beta=1/2$. The value of the average forcing is the same as in the blinking rotlet case, as is the mean deviation from the average value (indicated by the shaded area under the curves of Fig. 8). In Fig. 12, the evolution in time of a blob consisting of passive tracer particles is shown. Although the patterns look rather similar to the patterns due to the square wave forcing protocol, a significant difference can be seen from the more capricious form of the contours (see the upper region of the domain). This is also shown by calculating the relative length of the contour, which has been given in the caption of Fig. 12.

V. SUMMARY AND DISCUSSION

The slow viscous flow driven by one or two rotlets inside a rectangular cavity with nonmoving, impenetrable walls and variable aspect ratio is described by means of the stream function. The governing two-dimensional homogeneous biharmonic equation for the stream function has been solved analytically with use of the superposition principle. The flow was driven by a single rotlet on the y axis. Although the expression for the stream function does not have a closed form, an accurate description has been obtained in which the no-slip boundary conditions are satisfied at all four walls.

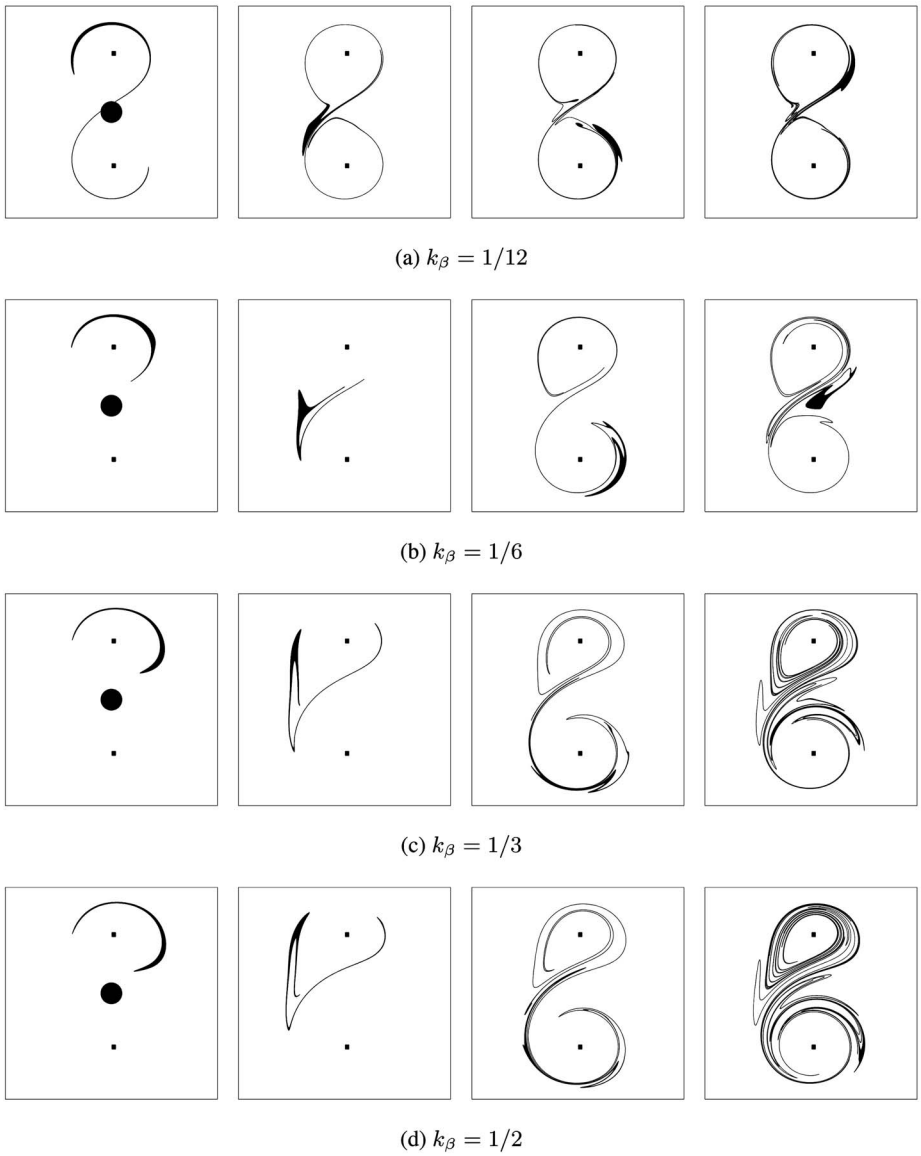

FIG. 11. Evolution of an initially circular blob containing passive tracer particles after several blinking periods (from left to right: T, $2T$, $3T$, and $4T$) for $\lambda_0=1/2$, $A_0=1/2$, and different values of the phase difference k_β. The position of the rotlets is indicated by dots.

The associated velocity field has not only been applied successfully to the description of the steady Stokes flow structures in slender rectangular cavities, but it has also been applied to chaotic transport of passive tracer particles in the case of a time-dependent forcing by a set of two blinking rotlets. The multicellular flow pattern that was observed in the first application was due to the rotation of a centrally located rotlet. An array of single-core cells appears in narrow cavity geometries of which the number is directly related to the domain aspect ratio A such that the number of cells increases for increasing A. The formation of the single-core cells involves the merging of the main corner cells (Moffatt eddies), which grow in size when the aspect ratio of the domain is increased and finally merge into a new, separated cell structure. This process continues when the domain is elongated even further, by which new cell structures are formed. Ultimately, this will lead to an infinitely large array of cells.[35] In this respect, the results are qualitatively comparable to those of a cylinder-driven cavity flow:[21] all the characteristic flow properties that we could expect were also found in the rotlet case. With two rotlets forcing the flow, the structure of the central cell was determined by the rotation direction of the rotlets.

In a second application, the transport of passive tracers is illustrated in the case of a time-dependent flow forcing. The symmetry of the problem made it possible to include a second rotlet, to a certain degree independently adjustable of the first one, into the cavity, forming a blinking rotlet pair. An important property of the flow in the rectangular domain, as was already reported for the circular domain,[1] is that the solution of the flow field allows for a rotlet position $(0,c_0)$ that generates a flow with a stagnation point $(0,-c_0)$ located symmetrically in the domain with respect to the x axis. By placing the rotlets in these special positions $(0,\pm c_0)$, the inactive rotlet does not disturb the flow generated by the active rotlet. An essential difference with the circular geometry is the existence of more than one of these special rotlet positions. The explanation for this lies in the presence of an array of single-core cells and the fact that these cells do not change position when the aspect ratio is further increased. Therefore, the number of these extra symmetric rotlet stag-

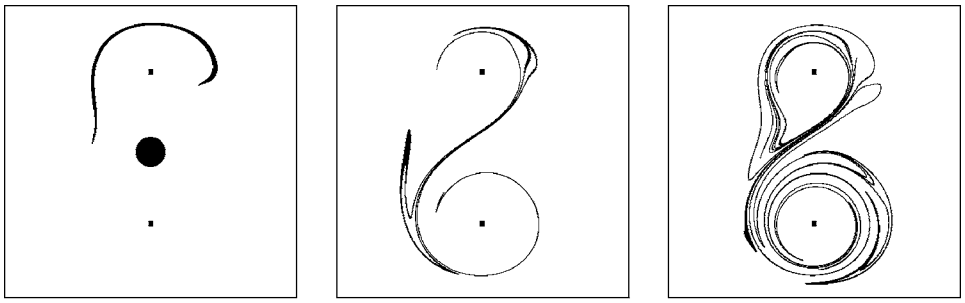

(a) Square wave time-dependent rotlet forcing

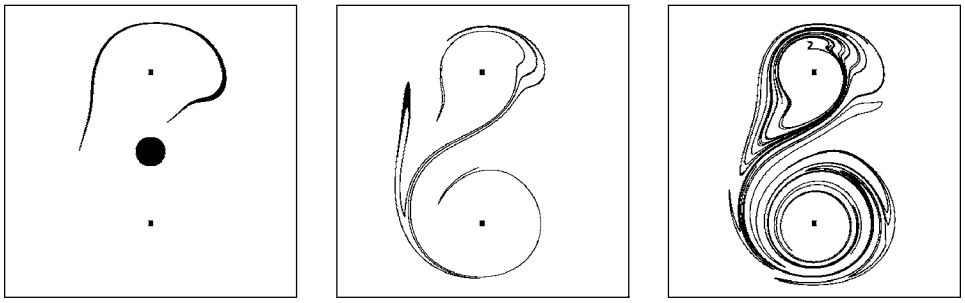

(b) Sine wave time-dependent rotlet forcing

FIG. 12. Evolution of an initially circular blob containing passive tracer particles after several periods (from left to right: T, $2T$, $3T$) for $k_\beta=1/2$. Comparison between a square wave time-dependent and sine wave time-dependent forcing protocol. The parameter set $\lambda_0=2/3$, $A_0=2/5$, and $A=\pi/5$ ensures "forcing area" preservation. The position of the rotlets is indicated by dots. The relative contour length reads $l(T)/l_0=5.8285$, $l(2T)/l_0=32.232$, and $l(3T)/l_0=200.12$ for the square wave; and $l(T)/l_0=7.4621$, $l(2T)/l_0=40.787$, $l(3T)/l_0=310.13$ for the sine wave.

nation point positions is related directly to the number of single-core cells present inside the domain and thus related to the aspect ratio. From this study, it can be concluded that stirring by two blinking rotlets in circular and square containers yields similar results despite the different container geometries. Moreover, the present computations clearly indicate that the best stirring (for the present parameter settings) is accomplished by perfect out-of-phase blinking rotlets where the sine-wave rotlet forcing gives better results than the square-wave rotlet forcing.

The stirring by rotlets is illustrated here by varying container geometry, rotlet positions, and blinking protocols. The present method enables further studies of mixing, although not pursued here, on measurements of spreading, such as, for instance, those based on using localized Lyapunov exponents.

A possible extension of this study concerns the implementation of the method introduced by Price *et al.*[25] for one or two real rotating cylinders in rectangular cavities. This requires designing and building a totally new numerical algorithm that takes into account both the no-slip boundary conditions at the cavity sidewalls and at the cylinder surfaces, which is a separate effort. However, if available it would allow a detailed comparison of the Stokes flow in rectangular cavities driven by real cylinders and those driven by rotlets, as discussed in the present paper, and to compare and analyze the advection properties of the flows driven by these different forcing mechanisms. Keeping in mind the remarkable qualitative agreement between the experimental and numerical results obtained by Hellou and Coutanceau,[21] based on a real cylinder and our results, based on a single rotlet in a rectangular cavity, it can be justified to restrict these investigations to the rotlet case for the moment and leave the challenging comparison with the method of Price *et al.* for future work.

ACKNOWLEDGMENT

We would like to thank Dr. Alexei Galaktionov for providing software to perform contour kinematics simulations.

[1] V. V. Meleshko and H. Aref, "A blinking rotlet model for chaotic advection," Phys. Fluids **8**, 3215 (1996); see also Erratum, *ibid.* **10**, 1543 (1998).
[2] G. K. Batchelor, *An Introduction to Fluid Dynamics* (Cambridge University Press, Cambridge, UK, 1967).
[3] G. Lamé, *Leçons sur la Théorie Mathématique de l'Elasticité des Corps Solides* (Bachelier, Paris, 1852).
[4] E. Mathieu, "Sur l'équilibre d'élasticité d'un prisme rectangle," Acad. Sci., Paris, C. R. **90**, 1272 (1880).
[5] E. Mathieu, "Mémoire sur l'équilibre d'élasticité d'un prisme rectangle," J. Ec. Polytech. (Paris) **30**, 173 (1881).
[6] E. Mathieu, *Théorie de l'Elasticité des Corps Solides* (Gauthiers-Villars, Paris, 1890).
[7] B. M. Koialovich, "On one partial differential equation of the fourth order," Doctoral dissertation, St-Petersburg University (1890) (in Russian); German review in J. Buch. Fortschr. Math. **33**, 367 (1902).
[8] I. G. Bubnov, "Stresses in the bottom plating of a ship due to water pressure," Mat. Sb. **312**, 119 (1902).
[9] I. G. Bubnov, *Structural Mechanics of a Ship* (Naval Academy Press, St. Petersburg, 1914), Vol. 2 (in Russian).
[10] G. Lauricella, "Sur l'intégration de l'équation relative à l'équilibre des plaques élastiques encastrées," Acta Math. **32**, 201 (1909).
[11] H. Hencky, "Der Spannungszustand in Rechteckigen Platten," Doctoral dissertation, Oldenburg, München und Berlin (1913).
[12] C. E. Inglis, "Stresses in rectangular plates clamped at their edges and loaded with a uniformly distributed pressure," Trans. RINA **67**, 147 (1925).
[13] K. Girkmann, *Flächentragwerke. Einführung in die Elastostatik der Scheiben, Platten, Schalen und Faltwerke*, 6th ed. (Springer-Verlag, Vienna, 1963).
[14] S. P. Timoshenko and S. Woinowski-Krieger, *Theory of Plates and Shells*, 2nd ed. (McGraw-Hill, New York, 1959).
[15] S. P. Timoshenko and J. N. Goodier, *Theory of Elasticity*, 3rd ed. (McGraw-Hill, New York, 1970).
[16] V. V. Meleshko, "Selected topics in the history of the two-dimensional biharmonic problem," Appl. Mech. Rev. **56**, 33 (2003).

[17] V. V. Meleshko, "Steady Stokes flow in a rectangular cavity," Proc. R. Soc. London, Ser. A **452**, 1999 (1996).
[18] T. S. Krasnopolskaya, V. V. Meleshko, G. W. M. Peters, and H. E. H. Meijer, "Steady Stokes flow in an annular cavity," Q. J. Mech. Appl. Math. **49**, 593 (1996).
[19] L. V. Kantorovich and V. I. Krylov, *Approximate Methods of Higher Analysis* (Noordhoff, Groningen, 1958).
[20] V. V. Meleshko and G. M. Gomilko, "Infinite systems for a biharmonic problem in a rectangle," Proc. R. Soc. London, Ser. A **453**, 2139 (1997).
[21] M. Hellou and M. Coutanceau, "Cellular Stokes flow induced by rotation of a cylinder in a closed channel," J. Fluid Mech. **236**, 557 (1992).
[22] S. C. Jana, G. Metcalfe, and J. M. Ottino, "Experimental and computational studies of mixing in complex Stokes flows: The vortex mixing flow and multicellular cavity flows," J. Fluid Mech. **269**, 199 (1994).
[23] H. Aref, "Stirring by chaotic advection," J. Fluid Mech. **134**, 1 (1984).
[24] S. R. Otto, A. N. Yannacopoulos, and J. R. Blake, "Transport and mixing in Stokes flow: The effect of chaotic dynamics on the blinking Stokeslet," J. Fluid Mech. **430**, 1 (2001).
[25] T. J. Price, T. Mullin, and J. J. Kobine, "Numerical and experimental characterization of a family of two-roll-mill flows," Proc. R. Soc. London, Ser. A **459**, 117 (2003).
[26] F. Moreau and J.-M. Bourot, "Ecoulements cellulaires de Stokes produits en canal plan illimité par la rotation de deux cylindres," ZAMP **44**, 777 (1993).
[27] E. Hairer, S. P. Nørsett, and G. Wanner, *Solving Ordinary Differential Equations I* (Springer-Verlag, Berlin, 1987).
[28] E. R. Hansen, *A Table of Series and Products* (Prentice-Hall, New York, 1975).
[29] F. Oberhettinger, *Fourier Expansions: A Collection of Formulas* (Academic, Englewood Cliffs, NJ, 1973).
[30] H. K. Moffatt, "Viscous and resistive eddies near a sharp corner," J. Fluid Mech. **18**, 1 (1964).
[31] W. R. Dean and P. E. Montagnon, "On the steady motion of viscous liquid in a corner," Proc. Cambridge Philos. Soc. **45**, 389 (1949).
[32] V. V. Meleshko, A. M. Gomilko, and A. A. Gourjii, "Normal reactions in a clamped elastic rectangular plate," J. Cell. Sci. **40**, 377 (2001).
[33] J. A. van de Konijnenberg, J. B. Flór, and G. J. F. van Heijst, "Decaying quasi-two-dimensional viscous flow on a square domain," Phys. Fluids **10**, 595 (1998).
[34] V. V. Meleshko and G. J. F. van Heijst, "Interacting two-dimensional vortex structures: Pint vortices, contour kinematics and stirring properties," Chaos, Solitons Fractals **4**, 977 (1994).
[35] W. W. Hackborn, "Asymmetric Stokes flow between parallel planes due to a rotlet," J. Fluid Mech. **218**, 531 (1990).